Key Points:
- A novel method for estimating the mesospheric wind field correlation and structure function from specular meteor trail echoes
- Spatial and temporal correlations of mesospheric wind fields are obtained with unprecedented coverage and resolution
- Structure functions of horizontal wind fluctuations in the horizontal and vertical directions show a −5/3 power spectral index

Correspondence to:
J. Vierinen,
jvi019@uit.no

Observing Mesospheric Turbulence With Specular Meteor Radars: A Novel Method for Estimating Second-Order Statistics of Wind Velocity

J. Vierinen[1] , J. L. Chau[2] , H. Charuvil[2,3], J. M. Urco[2] , M. Clahsen[2] , V. Avsarkisov[2] , R. Marino[3], and R. Volz[4]

[1]Department of Physics and Technology, University of Tromsø, The Arctic University of Norway, Tromsø, Norway, [2]Leibniz Institute of Atmospheric Physics, University of Rostock, Kühlungsborn, Germany, [3]Laboratoire de Mécanique des Fluides et d'Acoustique, CNRS, École Centrale de Lyon, Université Claude Bernard Lyon 1, INSA de Lyon, Écully, France, [4]Haystack Observatory, Massachusetts Institute of Technology, Westford, MA, USA

Abstract There are few observational techniques for measuring the distribution of kinetic energy within the mesosphere with a wide range of spatial and temporal scales. This study describes a method for estimating the three-dimensional mesospheric wind field correlation function from specular meteor trail echoes. Each radar echo provides a measurement of a one-dimensional projection of the wind velocity vector at a randomly sampled point in space and time. The method relies on using pairs of such measurements to estimate the correlation function of the wind with different spatial and temporal lags. The method is demonstrated using a multistatic meteor radar data set that includes $\approx 10^5$ meteor echoes observed during a 24-hr time period. The new method is found to be in good agreement with the well-established technique for estimating horizontal mean winds. High-resolution correlation functions with temporal, horizontal, and vertical lags are also estimated from the data. The temporal correlation function is used to retrieve the kinetic energy spectrum, which includes the semidiurnal mode and a 3-hr period wave. The horizontal and vertical correlation functions of the wind are then used to derive second-order structure functions, which are found to be compatible with the Kolmogorov prediction for spectral distribution of kinetic energy in the turbulent inertial range. The presented method can be used to extend the capabilities of specular meteor radars. It is relatively flexible and has a multitude of applications beyond what has been shown in this study.

1. Introduction

Characterizing the dynamic properties of a fluid equates to estimating the Reynolds stress tensor, that is, the correlation function $\langle u_\alpha u_\beta \rangle$ of velocity u_α, on a broad range of temporal and spatial scales. This quantity has so far not been exhaustively observed for the mesosphere. Especially lacking are measurements on spatial scales between regional and local. These scales are important for understanding the roles of various phenomena, such as coupling between different atmospheric layers, Rossby waves, tides, gravity waves, and turbulence modes within the mesosphere (e.g., Fritts & Alexander, 2003; Lindzen, 1981; Roberts & Larsen, 2014). For example, the body forces in the atmosphere are determined from the correlations between the vertical and horizontal wind components, that is, the vertical flux of the horizontal momentum (e.g., Lindborg & Cho, 2001).

In the mesosphere, the mean winds and wind correlations as function of altitude have been measured with various types of radars: medium frequency (MF), mesosphere stratosphere troposphere, specular meteor, and incoherent scatter (e.g., Fritts et al., 1992; Hocking, 2005; Nicolls et al., 2012; Vincent & Reid, 1983). These components have been also measured with lidars (e.g., Gardner & Yang, 1998). Wind correlations in the mesosphere were first measured by Vincent and Reid (1983) using an MF radar with pairs of co-planar narrow beams. The technique was later extended to an arbitrary number of pointing positions by Thorsen et al. (1997) using a wide-beam MF radar, and to all-sky monostatic specular meteor radars (SMRs) by Hocking (2005). The statistical uncertainties of the measured wind correlations have been studied by Kudeki and Franke (1998), Thorsen et al. (2000), and Nicolls et al. (2012), taking into account geophysical variability, spatial correlation, and the full covariance of line of sight velocities, respectively.

In all of these previous studies, estimates of wind correlation functions were obtained either by averaging over the whole observing volume (e.g., Andrioli et al., 2013; de Wit et al., 2014; Hocking, 2005; Placke et al., 2011; in the case of SMRs), or by sampling fixed spatial structures predetermined by the separation of relatively narrow beams used (e.g., Fritts et al., 1992, 2012;Nicolls et al., 2012; Placke et al., 2015, 2012; Sato et al., 2017, 2012; Vincent & Reid, 1983, 2012). In the case of wind correlations, the majority of these measurements have provided information about relatively small scale, or large scale correlations of the mesospheric wind field.

In some cases horizontal wavelengths were inferred from radar measurements, using the so-called "polarization relations" of gravity waves (e.g., Hines, 1960) and assuming a dominant monochromatic gravity wave for observed periods (e.g., Vincent & Reid, 1983). Horizontal scales of mesospheric waves have been also been obtained from observations of noctilucent clouds (e.g., Baumgarten & Fritts, 2014; Haurwitz & Fogle, 1969), mesospheric airglow emissions and temperatures (e.g., and references therein; Hecht et al., 2007; Pautet et al., 2016; Swenson et al., 1999), and luminescent chemical release experiments from rockets (e.g., Roberts & Larsen, 2014). These observations provide information on horizontal scales, but they are limited in both space and time. For example, noctilucent clouds can be only observed at high latitudes and during local summer. In the case of airglow observations, they are confined to clear-sky nights and the emission comes from a relative thick layer.

Being able to separate the temporal and spatial scales in the wind field correlation function is key to understanding mesospheric dynamics and the physical processes behind them. For example, according to theoretical studies the gravity wave part of the horizontal wind frequency spectra is expected to be proportional to T^p, where T is the period and p varies between 5/3 and 2 (e.g., Gardner et al., 1993). In the case of spatial spectra, the wavenumber spectra of the horizontal and vertical wind components due to gravity waves are expected to be proportional k_h^{-p} and k_w^{-p}, where $k_h = 2\pi/\lambda_h$ and $k_w = 2\pi/\lambda_z$ are the horizontal and vertical wavenumbers, respectively. The spectral index p is expected to be close to 5/3 for horizontal and 3 for vertical wind.

With observations of spatial and temporal correlation functions ranging across a wide range of spatial and temporal scales, one could also study and test whether the observed fluctuations are only related to divergent modes as commonly assumed or they are also the result of vortical modes, as it is expected from lower altitudes studies and direct numerical simulations (e.g., Lindborg, 2007; Marino et al., 2015). Similarly, one could determine a mesospheric equivalent to the tropospheric and stratospheric Nastrom and Gage (1985) spectrum . The simultaneous knowledge of spatial and temporal variations of the fields allows disentangling waves and turbulent motions and identifying the dispersion relation of gravity waves (e.g., Oks et al., 2017).

In Figure 1, we show a qualitative diagram of how energy is deposited and cascaded down to smallest scales in the mesosphere. The key assumption of this cascade mechanism is that there is a strongly stratified turbulence regime in the atmosphere (Billant & Chomaz, 2001; Brethouwer et al., 2007; Lindborg, 2006). This assumption has been recently verified with the use of the Kühlungsborn Mechanistic general Circulation Model. In particular, it was found that L_h should be around 150–200 km, while transition to Kolmogorov turbulence happens at scales $L_o = 60$–100 m. The Ozmidov scale L_o indicates transition to a pure vortex (turbulent) modes spectrum. In other words, gravity waves are not expected to contribute to the $-5/3$ energy spectrum at scales below 100 m. Finally, typical values for the buoyancy scale are $L_b = 7,001,000$ m. Buoyancy scale L_b is the largest vertical scale of turbulent structures in strongly stratified turbulence regime (not to confuse with Kolmogorov turbulence regime, for which L_o is the isotropic scale in all three directions). Using sounding rocket measurements from WADIS-2 rocket campaign it was found that the horizontal Froude numbers (Fr_h) in the winter mesosphere are 10^{-5}–10^{-2}. This result indicates that the winter mesosphere is in strongly stratified turbulence regime, since according to Lindborg (2006) this regime seem to emerge when Fr_h is below 0.02. All these theoretical, numerical, and observational results suggest that the mechanism shown in Figure 1 may play a relevant role in the winter mesosphere. Yet, questions on the directionality of the energy transfer in the mesosphere and in stratified geophysical flows in general (at the mesoscale and submesoscale) remain open (Marino et al., 2014; 2015).

In this study, we describe a novel method that aims at bridging the observational gap between large- and small-scale mesospheric wind fluctuations. We generalize previous approaches for measuring the wind field correlation function from radar measurements and show that products of one-dimensional measurements of the neutral wind (Doppler velocities) can be used to estimate the spatiotemporal correlation function
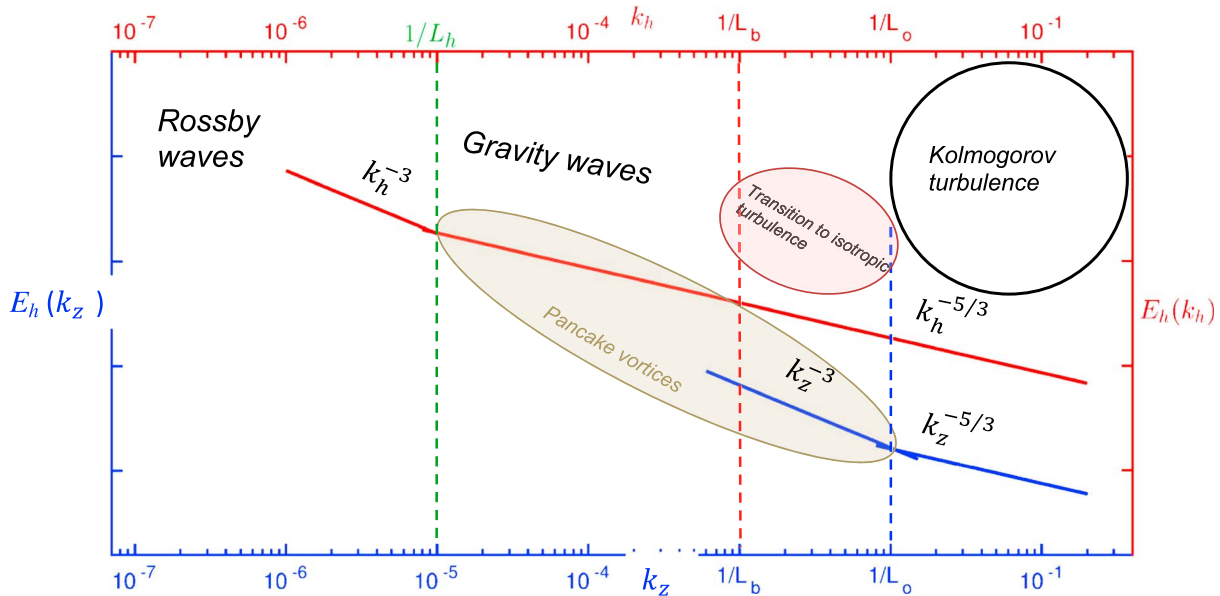
Figure 1. Simplified energy diagram describing a possible scenario in which regimes dominated by gravity waves, strongly stratified turbulence, and Kolmogorov turbulence are ideally well identified in the mesosphere. $L_h = \sigma_u^3/\epsilon$ is the outer horizontal scale of stratified turbulence. It is the largest horizontal scale of turbulent coherent structures that exist in the strongly stratified turbulence regime and are called pancake vortices. The outer horizontal scale also marks a transition of the horizontal energy spectra from gravity waves to strongly stratified turbulence. $L_b = \sigma_u/N$ is the buoyancy scale; it is the vertical outer scale of the pancake vortices. Transition to Kolmogorov turbulence happens at the Ozmidov scale $L_o = \sqrt{\epsilon/N^3}$. Thus, it is the outer scale for the three-dimensional Kolmogorov turbulent regime. σ_u, ϵ, and N are the root-mean-square wind velocity, the dissipation of kinetic energy, and the buoyancy frequency, respectively.

of the mesospheric wind field with a wide range of spatial and temporal scales, including scales of gravity waves and strongly stratified turbulence, also known as stratified macroturbulence. From the correlation functions, the frequency and wavenumber spectra can be obtained, as well as the second-order structure functions (e.g., Schulz-DuBois & Rehberg, 1981). The correlation function measurement principle is widely used in other geophysical fields, for example, meteorology, hydrology, oceanography, and space (e.g.,Kozelov & Golovchanskaya, 2006; Narita et al., 2011; Rhoads & Sukhodolov, 2004; Stull, 2012; Vogelzang et al., 2015). However, these methods typically operate on directly measured three-dimensional vector velocities, which cannot be measured using SMRs. The lack of direct unambiguous and simultaneous three-dimensional wind velocity measurements within a large enough geographic region has necessitated the development of an estimation method, which takes into account the sparse and incomplete nature of the observational data.

We apply our method to a unique data set obtained during a campaign where 12 bistatic SMR links have been employed. Multistatic geometries in SMRs were used recently to increase the number of meteor detections and obtain wind fields within large observing volumes (e.g., Chau et al., 2017; Stober & Chau, 2015; Stober et al., 2018). Multistatic geometries allow observing the same volume with different viewing angles, thus making possible the measurement of vorticity (e.g., Stober & Chau, 2015). The deployment of such types of networks is becoming easier and more feasible with the use of spread-spectrum (or coded continuous wave) and MIMO (multi-output and multi-input) concepts in atmospheric and ionospheric radars (e.g.,
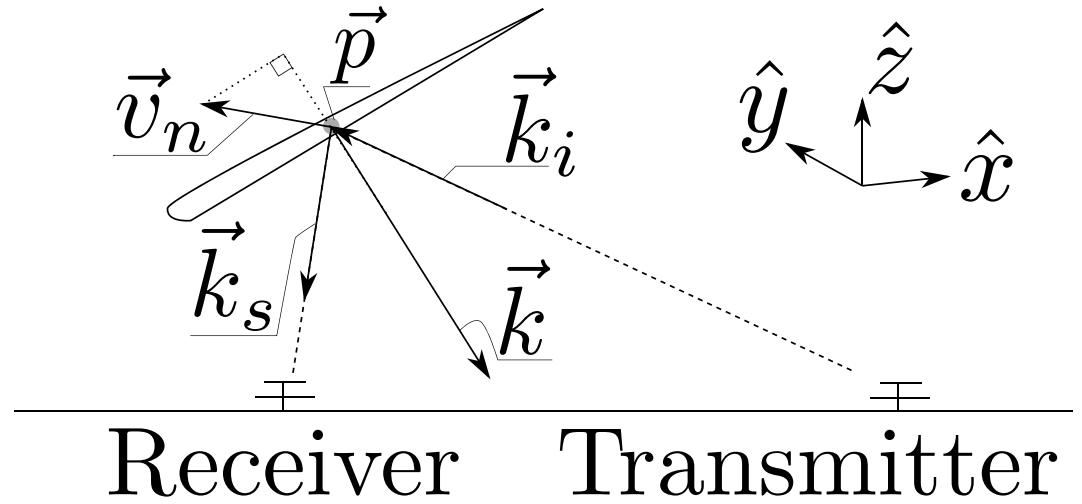
Figure 2. Geometry of a projected velocity of neutral wind, measured using a specular meteor trail echo observed with a bistatic radar, where $\vec{k}_i$, $\vec{k}_s$, and $\vec{k}$ are the incident, scattered, and Bragg wavevectors, respectively.

Chau et al., 2019; Hysell et al., 2016; Urco, Chau, Milla, et al. 2018; Urco, Chau, Weber, et al.,2018; Vierinen et al., 2016).

We validate our method against a well-established approach for the estimation of the mean horizontal winds (e.g., Hocking et al., 2001; Holdsworth et al., 2004). We then demonstrate the applicability of our method for studying the correlation and second-order structure function of the mesospheric wind in temporal, horizontal, and vertical dimensions.

2. Methods

SMRs measure the Doppler shift f_d of meteor trails, which drift in the mesospheric neutral wind. For specular meteor trail scattering, the measured Doppler shift is a one-dimensional projection of the three-dimensional neutral wind vector $\vec{v}_n(\vec{p})$ at the specular reflection point located at position $\vec{p}$:

$$-\omega_r = -2\pi f_d = \vec{k} \cdot \vec{v}_n(\vec{p}) \ (\text{rad/s}). \tag{1}$$

Here $\vec{k} = \vec{k}_s - \vec{k}_i$ is the Bragg wave vector, which is obtained from the incident ($\vec{k}_i$) and scattered ($\vec{k}_s$) wave vectors. The geometry of an individual measurement is shown in Figure 2. Interferometric SMRs measure the location $\vec{p}$ of the trail echo, which allows determining $\vec{k}$. The location is obtained by combining radio wave propagation time with interferometric means for measuring angle of arrival of the echo. We have recently demonstrated that it is possible to also use angle of departure with multiple interferometric transmit antennas (e.g., Chau et al., 2019).

The wind vector $\vec{v}_n(t, \vec{p})$ at any given position $\vec{p}$ and time t can be represented using the local meteor-centered East-North-Up (ENU) Cartesian coordinate system as follows:

$$\vec{v}_n(t, \vec{p}) = u(t, \vec{p})\hat{\boldsymbol{x}}(\vec{p}) + v(t, \vec{p})\hat{\boldsymbol{y}}(\vec{p}) + w(t, \vec{p})\hat{\boldsymbol{z}}(\vec{p}). \tag{2}$$

Here $\hat{\boldsymbol{x}}(\vec{p})$, $\hat{\boldsymbol{y}}(\vec{p})$, and $\hat{\boldsymbol{z}}(\vec{p})$ represent the unit vectors of the east, north, and up directions located at position $\vec{p}$, and $u(t, \vec{p})$, $v(t, \vec{p})$, and $w(t, \vec{p})$ are the three components of the neutral wind. We use occasionally also u_α notation to conveniently refer to the three components of the wind in general. In this case, the subscript α refers to one of the three velocity components.

To compress the notation further, let us combine the unit vectors for the meteor-centered ENU coordinate system with $\vec{k}$, which is also in the same meteor-centered ENU coordinate system:

$$k^x = \vec{k} \cdot \hat{\boldsymbol{x}}(\vec{p}) \quad k^y = \vec{k} \cdot \hat{\boldsymbol{y}}(\vec{p}) \quad k^z = \vec{k} \cdot \hat{\boldsymbol{z}}(\vec{p}) \tag{3}$$

A measurement of Doppler shift r, including measurement error ξ, can be written as

$$
\begin{aligned}
r &= -\omega_r + \xi \\
&= \vec{k} \cdot \vec{v} + \xi \\
&= u(t,\vec{p})k^x + v(t,\vec{p})k^y + w(t,\vec{p})k^z + \xi.
\end{aligned}
\tag{4}
$$

We assume that the measurement error ξ is a zero-mean independent normally distributed random variable.

2.1. Wind Field Correlation Function Inversion

In this section, we describe how the lag-product velocity measurements can be used to estimate the correlation function of the wind field. Hereafter we refer to this as the wind field correlation function inversion (WCFI) method.

We start with two measurements of Doppler shift (r_i and r_j), observed at times t_i and t_j, and positions $\vec{p}_i$ and $\vec{p}_j$:

$$
\begin{aligned}
r_i &= u(t_i,\vec{p}_i)k_i^x + v(t_i,\vec{p}_i)k_i^y + w(t_i,\vec{p}_i)k_i^z + \xi_i \\
r_j &= u(t_j,\vec{p}_j)k_j^x + v(t_j,\vec{p}_j)k_j^y + w(t_j,\vec{p}_j)k_j^z + \xi_j
\end{aligned}
$$

We then take the product of these two measurements and obtain

$$
\begin{aligned}
r_i r_j =\,& u(t_i,\vec{p}_i)u(t_j,\vec{p}_j)k_i^x k_j^x + u(t_i,\vec{p}_i)v(t_j,\vec{p}_j)k_i^x k_j^y + u(t_i,\vec{p}_i)w(t_j,\vec{p}_j)k_i^x k_j^z + \\
& v(t_i,\vec{p}_i)u(t_j,\vec{p}_j)k_i^y k_j^x + v(t_i,\vec{p}_i)v(t_j,\vec{p}_j)k_i^y k_j^y + v(t_i,\vec{p}_i)w(t_j,\vec{p}_j)k_i^y k_j^z + \\
& w(t_i,\vec{p}_i)u(t_j,\vec{p}_j)k_i^z k_j^x + w(t_i,\vec{p}_i)v(t_j,\vec{p}_j)k_i^z k_j^y + w(t_i,\vec{p}_i)w(t_j,\vec{p}_j)k_i^z k_j^z + \\
& + u(t_i,\vec{p}_i)k_i^x \xi_j + v(t_i,\vec{p}_i)k_i^y \xi_j + w(t_i,\vec{p}_i)k_i^z \xi_j \\
& + u(t_j,\vec{p}_j)k_j^x \xi_i + v(t_j,\vec{p}_j)k_j^y \xi_i + w(t_j,\vec{p}_j)k_j^z \xi_i \\
& + \xi_i \xi_j
\end{aligned}
\tag{5}
$$

Of these terms, the top three rows contain information about the wind velocity correlations, and the bottom three rows are zero-mean random variables. The mesospheric wind vector can be modeled as a stationary and horizontally homogenous stochastic process, and therefore, the terms u, v, and w are random variables. We assume them to be Gaussian random variables with some unknown correlation, which we want to estimate. The expected values of the products of the random variables can be expressed as a correlation function $G_{\alpha\beta}(\tau,\vec{s})$, which is a function of temporal and spatial displacement. Due to symmetry, there are six unique combinations of the wind components:

$$
\langle u(t_i,\vec{p}_i)u(t_j,\vec{p}_j)\rangle = G_{uu}(\tau,\vec{s})
\tag{6}
$$

$$
\langle v(t_i,\vec{p}_i)v(t_j,\vec{p}_j)\rangle = G_{vv}(\tau,\vec{s})
\tag{7}
$$

$$
\langle w(t_i,\vec{p}_i)w(t_j,\vec{p}_j)\rangle = G_{ww}(\tau,\vec{s})
\tag{8}
$$

$$
\langle u(t_i,\vec{p}_i)v(t_j,\vec{p}_j)\rangle = G_{uv}(\tau,\vec{s})
\tag{9}
$$

$$
\langle u(t_i,\vec{p}_i)w(t_j,\vec{p}_j)\rangle = G_{uw}(\tau,\vec{s})
\tag{10}
$$

$$
\langle v(t_i,\vec{p}_i)w(t_j,\vec{p}_j)\rangle = G_{vw}(\tau,\vec{s})
\tag{11}
$$

The correlation function $G_{\alpha\beta}(\tau,\vec{s})$ is a function of spatial and temporal displacement $\tau = t_i - t_j$ and $\vec{s} = \vec{p}_i - \vec{p}_j$. For example, $G_{uu}(\tau,0)$ would be the temporal autocorrelation function of the zonal component of neutral wind with no displacement in space. Similarly, $G_{vv}(0,\vec{s})$ would measure the spatial autocorrelation function of the meridional component of the wind field at a spatial displacement indicated by $\vec{s}$ and no displacement in time.

If we form a cross product between the Doppler shifts of two different meteor echoes, we can relate a pair of two different measurements multiplied with one another with the correlation function of the wind:

$$
m_{ij} = r_i r_j = \langle r_i r_j \rangle + \zeta,
\tag{12}
$$

where $\langle r_i r_j \rangle$ is the expected value of the product of two Doppler shift measurements r_i and r_j. We use $m_{ij} = r_i r_j$ to denote a pair of Doppler velocity measurements that have been multiplied together. We will call such a measurement a lag-product measurement, because measurements i and j are inevitably displaced by a certain temporal and spatial lag when $i \neq j$. The term ζ is a zero-mean random variable associated to the expected statistical uncertainty. This random variable is not normally distributed, but it has a symmetric distribution centered around zero when $i \neq j$.

To estimate the correlation function for a given value of τ and $\vec{s}$, we need to use a large number of measurements with similar temporal τ and spatial displacements $\vec{s}$, and binned in such a way that they originate from a region of interest in space and time. For example, we could use a selection criteria that requires the first measurement to (1) occur within 1-hr from noon and (2) occur between 92 and 93 km. The second measurement could be required to be (1) displaced in time by at most 60 s, (2) displaced horizontally by at most 20 km in distance, and (3) displaced by at most 1 km in the vertical direction.

While these sorts of selection criteria limit the number of lagged-product measurement pairs that can be used, SMRs are operated continuously, observing tens of thousands of meteors per day. When estimating the wind field correlation, it is also possible to collect measurements that satisfy the criteria of interest over a long period of time. For N measurements, we can form $M = N(N-1)/2$ unique pairs of measurements m_{ij}, so the number of measurements that can be obtained during several days of measurements is relatively large, even with relatively strict selection criteria. We discuss this in more detail in section 3.1.

The products of pairs of measurements can be expressed as a linear equation:

$$\boldsymbol{m} = \boldsymbol{A}\boldsymbol{x} + \boldsymbol{\xi} \tag{13}$$

$$
\begin{bmatrix}
m_{12} \\
m_{13} \\
m_{14} \\
\vdots \\
m_{ij}
\end{bmatrix}
=
\begin{bmatrix}
k_1^x k_2^x & k_1^y k_2^y & k_1^z k_2^z & (k_1^x k_2^y + k_1^y k_2^x) & (k_1^x k_2^z + k_1^z k_2^x) & (k_1^y k_2^z + k_1^z k_2^y) \\
k_1^x k_3^x & k_1^y k_3^y & k_1^z k_3^z & (k_1^x k_3^y + k_1^y k_3^x) & (k_1^x k_3^z + k_1^z k_3^x) & (k_1^y k_3^z + k_1^z k_3^y) \\
k_1^x k_4^x & k_1^y k_4^y & k_1^z k_4^z & (k_1^x k_4^y + k_1^y k_4^x) & (k_1^x k_4^z + k_1^z k_4^x) & (k_1^y k_4^z + k_1^z k_4^y) \\
\vdots & & & & & \\
k_i^x k_j^x & k_i^y k_j^y & k_i^z k_j^z & (k_i^x k_j^y + k_i^y k_j^x) & (k_i^x k_j^z + k_i^z k_j^x) & (k_i^y k_j^z + k_i^z k_j^y)
\end{bmatrix}
\begin{bmatrix}
G_{uu} \\
G_{vv} \\
G_{ww} \\
G_{uv} \\
G_{uw} \\
G_{vw}
\end{bmatrix},
\tag{14}
$$

where $\boldsymbol{m} \in \mathbb{R}^{M \times 1}$ is a vector of measurements, $\boldsymbol{A} \in \mathbb{R}^{M \times 6}$ is the theory matrix, $\boldsymbol{x} \in \mathbb{R}^{6 \times 1}$ is a vector containing the correlations, and $\boldsymbol{\xi} \in \mathbb{R}^{M \times 1}$ is a vector with measurement errors.

It is now possible to estimate the correlation function by obtaining a linear least squares estimate of x.

$$\boldsymbol{x}_{LS} = (\boldsymbol{A}^T \Sigma^{-1} \boldsymbol{A})^{-1} \boldsymbol{A}^T \Sigma^{-1} \boldsymbol{m}. \tag{15}$$

Note that it is only possible to use this equation directly if there is only a small number of measurements. An iterative solver is needed when the number of measurements grows large. Since the noise is non-Gaussian, the least squares estimate is not a maximum likelihood estimate, but it works well in practice.

If the covariance structure of the measurement errors ˝ is unknown, it is possible to use an identity matrix:

$$\Sigma = \boldsymbol{I}, \tag{16}$$

In most cases, two different lagged-product measurements are correlated, because the mesospheric winds are correlated over long periods of time. However, characterizing the true covariance of measurement errors requires knowing the correlation function of the mesospheric winds in advance. Therefore, in order to obtain realistic measurement errors, it is possible to use a two step procedure, where the identity matrix error covariance matrix is first used to estimate the correlation function of the mesospheric wind, and then use the estimated correlation function as input to a second linear least square estimate, which uses a more correct measurement error covariance matrix Σ, as discussed by Nicolls et al. (2012).

2.2. Sampling

SMRs detect a variable amount of meteors per unit of time at different times of the day. This is due to observing geometry combined with the meteor source distribution (e.g., Chau et al., 2017; Younger et al., 2009). The variable count of meteors per unit of time results in an uneven sampling of meteor wind as a function of time. If one aims to estimate the average correlation function over, say, 24 hr, then one needs to weight

observations based on the meteor detection rate at different times of day, in order to evenly average the mesospheric wind field characteristics over this observation period.

If there are N_i pairs of lag-product measurements per unit time at time t_i, then pairs of observations at time t_i need to be inversely weighted with $\gamma_{ij} = N_i^{-1}$. This can be achieved by using a diagonal measurement error covariance matrix

$$\Sigma = \mathrm{diag}(\gamma_{12}^{-2}, \gamma_{13}^{-2}, \dots, \gamma_{ij}^{-2}) \tag{17}$$

when estimating the correlation function.

Such weighting does not give exactly even weights to all times of day, as the "perfectly even" weighting also depends on the k-vectors that go into the theory matrix. However, the weighting strategy outlined above is somewhat straightforward to implement and still gives nearly even weight to all periods of time.

2.3. Fluctuating Wind

The Reynolds decomposition divides a wind into the mean and fluctuating components; that is,

$$u_\alpha = \bar{u}_\alpha + u'_\alpha. \tag{18}$$

Here u_α is the wind velocity, $\bar{u}_\alpha = \langle u_\alpha \rangle$ is the mean wind, and u'_α is the fluctuating component. This definition depends strongly on the definition of the averaging operation. The mean wind is different when averaging over 1 month, 24 hr, or 15 min. The mean wind also depends on the spatial extent of the averaging operation. The definition of the mean wind is therefore case specific.

A straightforward way to use the WCFI method for estimating mean and fluctuating components is to estimate two different correlation functions. One that estimates the mean correlation function over a large spatial or temporal extent $\bar{G}_{\alpha\beta}$ (see section 2.4), and one that estimates the correlation function over a small spatial and temporal extent: $G_{\alpha\beta}$. The difference between these two is the correlation function of the fluctuating component $G'_{\alpha\beta} = G_{\alpha\beta} - \bar{G}_{\alpha\beta}$. This however requires very long averaging times to obtain sufficiently small errors for small-magnitude features to be statistically significant, especially when the mean wind magnitude is significantly larger than the fluctuating component.

In some cases, it is possible to identify high- and low-frequency components of the wind directly from the full-correlation function $G_{\alpha\beta}$, provided that a sufficiently wide range of temporal and spatial lags are estimated, so that different wave modes of the wind field can be identified. Short lags contain contributions from the mean and fluctuating components, whereas the long lags consist of mainly the mean wind.

Sometimes it is advantageous to only estimate the high-frequency spatiotemporal components of the wind by filtering out the mean winds from the measurements first (Stull, 2012). The fluctuating components u'_α consist of high spatiotemporal frequency wave modes and the mean wind consists of low spatiotemporal frequency waves. In order to high-pass filter the measurements, one can subtract the mean wind from the projected Doppler velocity measurements as follows:

$$\begin{aligned} r'_i &= r_i - \bar{u}(t_i, \vec{p}_i)k_i^x - \bar{v}(t_i, \vec{p}_i)k_i^y - \bar{w}(t_i, \vec{p}_1)k_i^z \\ &= u'(t_i, \vec{p}_i)k_i^x + v'(t_i, \vec{p}_i)k_i^y + w'(t_i, \vec{p}_i)k_i^z + \xi_i, \end{aligned} \tag{19}$$

where r_i is the Doppler shift measurement. The term $\bar{u}_\alpha$ is the mean wind estimate, which can be obtained using the standard linear least squares estimation method (e.g., Hocking et al., 2001; Holdsworth et al., 2004). The mean wind estimation (MWE) method is also described in section 2.5. The error term ξ_i contains contributions from Doppler velocity measurement errors and errors associated with MWE. After subtracting the mean wind component from the measurements, one obtains a measurement r'_i, which is a Doppler shift measurement of the high-pass-filtered wind.

It is then possible to use the high-pass-filtered lag-product measurements $m_{ij} = r'_i r'_j$ and proceed with the WCFI method as outlined earlier in this section to determine the correlation function of the fluctuating component of the wind: $G'_{\alpha\beta} = \langle u'_\alpha u'_\beta \rangle$. If necessary, this can be combined with the mean wind to obtain the full-correlation function that also contains the mean wind:

$$\begin{aligned} G_{\alpha\beta} &= G'_{\alpha\beta} + \langle \bar{u}_\alpha \bar{u}_\beta \rangle \\ &= G'_{\alpha\beta} + \bar{G}_{\alpha\beta} \end{aligned} \tag{20}$$

This relies on the assumption that $\langle u'_\alpha \bar{u}_\beta \rangle = 0$, that is, that the fluctuating component of the wind is uncorrelated with the mean wind.

The advantage of using high-pass-filtered measurements is that the measurements have a shorter temporal and spatial correlation length, which allows more independent samples of the wind field correlation function to be obtained per unit of time and space. High-pass filtering also reduces self-noise with long temporal correlations.

One complication that arises when applying a high-pass filter to the data is that it can result in complicated frequency response characteristics, which makes interpretation of measurements less straightforward.

2.4. Mean Wind Correlation Function Estimation

The WCFI method can be used to estimate the mean wind correlation function. In order to do this, we must make the assumption that the wind correlation function is the same across a large spatial and temporal extent. In this case, the fluctuating component of the wind behaves to first order like zero-mean independent random variables, which can be grouped together with measurement errors:

$$
\begin{aligned}
r_i &= \bar{u}(t_i, \vec{p}_i)k_i^x + \bar{v}(t_i, \vec{p}_i)k_i^y + \bar{w}(t_i, \vec{p}_i)k_i^z + r_i' + \xi_i \\
&= \bar{u}(t_i, \vec{p}_i)k_i^x + \bar{v}(t_i, \vec{p}_i)k_i^y + \bar{w}(t_i, \vec{p}_i)k_i^z + \xi_i',
\end{aligned}
\tag{21}
$$

Here $\xi_i' = r_i' + \xi_i$ is a zero-mean random variable, which includes contributions from measurement errors and the fluctuating component of the wind. This is only valid, if the spatial and temporal volumes that are being correlated are sufficiently large that the fluctuating component is decorrelated ($\langle \xi i' \xi j' \rangle \approx 0$).

2.5. Mean Wind Amplitude Estimation

The standard MWE method (e.g., Hocking et al., 2001; Holdsworth et al., 2004) is routinely used by SMRs to estimate the mean horizontal wind velocity. This estimate is obtained by assuming that the wind across all of the measurements at a similar altitude over a short period of time is described by

$$
\vec{v}_n = \bar{u}\hat{\boldsymbol{x}} + \bar{v}\hat{\boldsymbol{y}} + u'\hat{\boldsymbol{x}} + v'\hat{\boldsymbol{y}} + w'\hat{\boldsymbol{z}}
\tag{22}
$$

where $\bar{u}$, $\bar{v}$ are the mean horizontal wind components in the x and y directions. The fluctuating components u', v', and w' are assumed to be zero-mean Gaussian random variables. The mean vertical wind is assumed to be zero. It is also possible to include zonal and meridional gradients of the mean wind, as discussed by Chau et al. (2017).

The relationship between measured projected velocities and the mean horizontal wind is linear:

$$
\begin{aligned}
r &= \vec{k} \cdot \vec{v}_n + \xi_d \\
&= k^x \bar{u} + k^y \bar{v} + \xi.
\end{aligned}
\tag{23}
$$

The sum of the contributions of the fluctuating wind components and the Doppler velocity measurement error ξ_d is assumed to be a zero-mean Gaussian random variable

$$
\xi = \vec{k} \cdot (u'\hat{\boldsymbol{x}} + v'\hat{\boldsymbol{y}} + w'\hat{\boldsymbol{z}}) + \xi_d.
\tag{24}
$$

The contributions of the fluctuating wind and the measurement errors for each measurement can be treated as a zero-mean independent and identically distributed Gaussian random variables.

This measurement equation can be expressed in matrix form for a large number of measurements that are closely spaced in altitude and time as

$$
\boldsymbol{m} = \boldsymbol{Ax} + \boldsymbol{\xi}
$$

$$
\begin{bmatrix} r_1 \\ r_2 \\ \vdots \\ r_N \end{bmatrix} = \begin{bmatrix} k_1^x & k_1^y \\ k_2^x & k_2^y \\ \vdots \\ k_N^x & k_N^y \end{bmatrix} \begin{bmatrix} \bar{u} \\ \bar{v} \end{bmatrix} + \boldsymbol{\xi}.
$$

Using linear least squares, one can obtain an estimate of the two unknowns (mean horizontal wind components), provided that there are sufficient observations. The maximum likelihood estimator for these parameters is

$$\mathbf{x}_{ML} = (\mathbf{A}^T \Sigma^{-1} \mathbf{A})^{-1} \mathbf{A}^T \Sigma^{-1} \mathbf{m}. \tag{25}$$

Here Σ is the covariance matrix that describes the error covariance structure of the projected wind field measurement errors $\langle \xi \xi^T \rangle$. The estimation errors for mean wind can be obtained with:

$$\Sigma_p = (\mathbf{A}^T \Sigma^{-1} \mathbf{A})^{-1}. \tag{26}$$

We assume that each measurement is statistically independent, and the covariance matrix of measurements can be estimated from the residuals of the fit, to obtain a realistic estimate of MWE errors.

2.6. Self-Product Measurements

It is also possible to form lagged-product measurements of the same Doppler velocity measurement $m_{ii} = r_i r_i$ and use them when estimating the zero-lag of the correlation function. This type of measurement can be advantageous, as it provides a measurement of the correlation function with zero displacement in space and time. The obtained correlation functions would contain the average of all the scales within the observing volume and time span. If the mean components (e.g., planetary waves and tides) are removed from the Doppler velocity measurements ($m_{ii} = r_i' r_i'$), these estimates include statistical information about short temporal and spatial scale gravity waves. The Hocking (2005) method for estimating momentum flux utilizes only high-pass-filtered measurements of form $m_{ii} = r_i' r_i'$.

These types of zero-lag measurement pairs have one important complication. The Doppler velocity measurement errors are correlated for the self-product $r_i r_i$. This means that the last term $\xi_i \xi_j$ in equation (5) is not a zero-mean random variable ($\langle \xi_i \xi_i \rangle \neq 0$). If the Doppler velocity measurement error variance is not subtracted from the lagged-product measurements, the estimate of the correlation function is biased. This is the case also with high-pass filtered Doppler velocity measurements. The bias is largest when the magnitude of the correlation function is small. If the variance of the measurement errors is significantly smaller than the magnitude of the correlation function that is estimated, the bias will be minimal.

In order to reduce the uncertainties on parameters resulting from self-product measurements, Nicolls et al. (2012) proposed a method that utilized also the full-correlation (including $i \neq j$ pairs) of distributed radial velocity measurements. In principle, the proposed method uses the same full-correlation matrix that we used in our WCFI method, but $i \neq j$ pairs are not used to exploit the spatial and temporal information they contain. The method was especially suitable for estimates of higher-frequency wave motions and was applied to a fixed number of beam positions at the Poker Flat incoherent scatter radar.

2.7. Lags and Lag Resolution

The basic principle behind correlation function inversion is measuring correlations between the wind vector field in space and time. The lag depends on the measurement pairs $m_{ij} = r_i r_j$ that are used to estimate the correlation function. Therefore, estimation of a certain temporal and spatial lag involves a selection of measurements that have similar temporal and spatial displacements. This can be done is several different ways. We will describe one method.

Let us define a four-dimensional set, which limits the positions of measurements in time and space: $t_i \in T_0, \vec{p}_i \in V_0$. The first set determines the four-dimensional volume over which the correlation function is to be estimated in. The first measurement r_i of a lagged-product measurement m_{ij} is selected from this set. The first set can, for example, be within 30 min from noon, between 91 and 92 km in altitude, and with any horizontal location.

For each measurement i in set T_0, V_0, one finds another set of measurements $t_j \in T_i, \vec{p}_j \in V_i$, which have temporal and spatial displacements that are close to the temporal and spatial lags τ and $\vec{s}$ that are to be estimated. The second pair of each lagged-product measurements r_j is selected from this set (T_i, V_i). For example, the set (T_i, V_i) could be used to specify that the time of the second measurement t_j should be displaced by between 60 and 120 s in time relative to t_i ($t_i + 60 < t_j < t_i + 120$), the position $\vec{p}_j$ displaced by less than 50 km in horizontal distance and by less than 1 km in vertical distance relative to $\vec{p}_i$.

The correlation function estimate is then a measure of the following matrix:

$$\Sigma_v(\tau, \vec{s}) = \langle \vec{v}_n(t_i \in T_0, \vec{p}_i \in V_0) \vec{v}_n(t_j \in T_i, \vec{p}_j \in V_i)^T \rangle. \tag{27}$$

The terms in the matrix are the correlation functions at lag τ and $\vec{s}$:

$$\Sigma_v(\tau, \vec{s}) = \begin{bmatrix} G_{uu}(\tau, \vec{s}) & G_{uv}(\tau, \vec{s}) & G_{uw}(\tau, \vec{s}) \\ G_{uv}(\tau, \vec{s}) & G_{vv}(\tau, \vec{s}) & G_{vw}(\tau, \vec{s}) \\ G_{uw}(\tau, \vec{s}) & G_{vw}(\tau, \vec{s}) & G_{ww}(\tau, \vec{s}). \end{bmatrix} \tag{28}$$

The spatial and temporal lags are the mean values of the temporal and spatial displacements of the lagged-product measurements: $\tau = \langle t_i - t_j \rangle$ and $\vec{s} = \langle \vec{p}_i - \vec{p}_j \rangle$. The averaging is done over all combinations of (i, j) that are used to estimate the correlation function for this lag.

It is often advantageous to divide the spatial lag into horizontal and vertical components, because horizontal and vertical directions have different scale lengths:

$$\vec{p}_i - \vec{p}_j = d_{ij,x}\hat{x} + d_{ij,y}\hat{y} + d_{ij,z}\hat{z}. \tag{29}$$

In this way, we can divide the spatial lag into zonal and meridional lags $s_x = \langle d_{ij,x} \rangle$ and $s_y = \langle d_{ij,y} \rangle$, and a vertical lag $s_z = \langle d_{ij,z} \rangle$. We can also use horizontal lags in arbitrary directions with $s_h = \langle (d_{ij,x}^2 + d_{ij,y}^2)^{1/2} \rangle = \langle d_{ij,h} \rangle$.

In practice, there are only a finite number of measurements that can be used. In order to have a sufficient number of lagged-products of measurements for estimating a certain lag, one needs to also define the lag resolution. The spatial and temporal resolution be defined as the maximum allowable deviation from the lag that is being estimated. These can be specified as $\Delta\tau = 2\max(|t_i - t_j - \tau|)$, $\Delta s_x = 2\max(|d_{ij,x} - s_x|)$, $\Delta s_y = 2\max(|d_{ij,y} - s_y|)$, $\Delta s_h = 2\max(|d_{ij,h} - s_h|)$, and $\Delta s_z = 2\max(|d_{ij,z} - s_z|)$. It is this lag resolution that determines the sizes of the sets T_i, V_i.

Figure 3 illustrates two different cases of measurement selection for spatial lags. Figure 3a shows the relationship of measurement i to the set V_i corresponding to a lag $\vec{s}$ and lag resolutions Δs_x, Δs_y, and Δs_z. Figure 3b shows the selection criteria for measurements that are used to determine a horizontal lag s_h with an arbitrary direction, a horizontal lag resolution Δs_h and a vertical lag resolution Δs_z.

Inspecting a certain feature of the wind field involves identifying temporal and spatial lags $\tau, \vec{s}$, which provide useful information about the phenomena that is studied. It is also important to choose a temporal and spatial resolution ($\Delta\tau$, Δs_h, Δs_x, Δs_y, and Δs_z) that matches the scale size that is being studied, while also providing a sufficient number of lagged-product measurements to allow a good estimate of that lag to be obtained. The correlation function estimate for a certain lag is averaged over the temporal and spatial scale determined by the lag resolution. For example, in order to be able to observe 200-s temporal wave fluctuations and 100-km horizontal wave fluctuations, $\Delta\tau$ needs to be less than 100 s and $\Delta s_h < 50$ km, due the Shannon-Nyquist sampling theorem.

We know that there are spatial and temporal correlations within mesospheric winds. Rossby waves, tides, gravity waves, and turbulence have correlations ranging from seconds and meters to weeks and thousands of kilometers. Being able to measure the six components of the wind field correlation function at different spatial and temporal lags allows us to quantify these correlations, which yields statistical information about the neutral dynamics. SMRs are useful tools exactly for this purpose, as meteors enter the atmosphere at random positions and times, allowing statistically a wide range of spatial and temporal lags to be observed with good lag resolution, as long as a sufficiently long time span is used to average the correlation function.

2.8. Relationship to the Structure Function

Assuming that the wind field is a wide sense stationary and horizontally homogeneous random process, we can relate the correlation function $G_{\alpha\beta}$ to the second-order structure function (Frisch, 1995; Kolmogorov, 1941; Schulz-DuBois & Rehberg, 1981; Tatarskii, 1961), hereafter referred as the "structure function." The structure function for a pair of wind components u_α and u_β, measured at times t and t' in positions $\vec{p}$ and $\vec{p}'$ is defined as follows:

$$S_{\alpha\beta}(\tau, \vec{s}) = \langle [u_\alpha(t, \vec{p}) - u_\beta(t', \vec{p}')]^2 \rangle \tag{30}$$

a)

b)
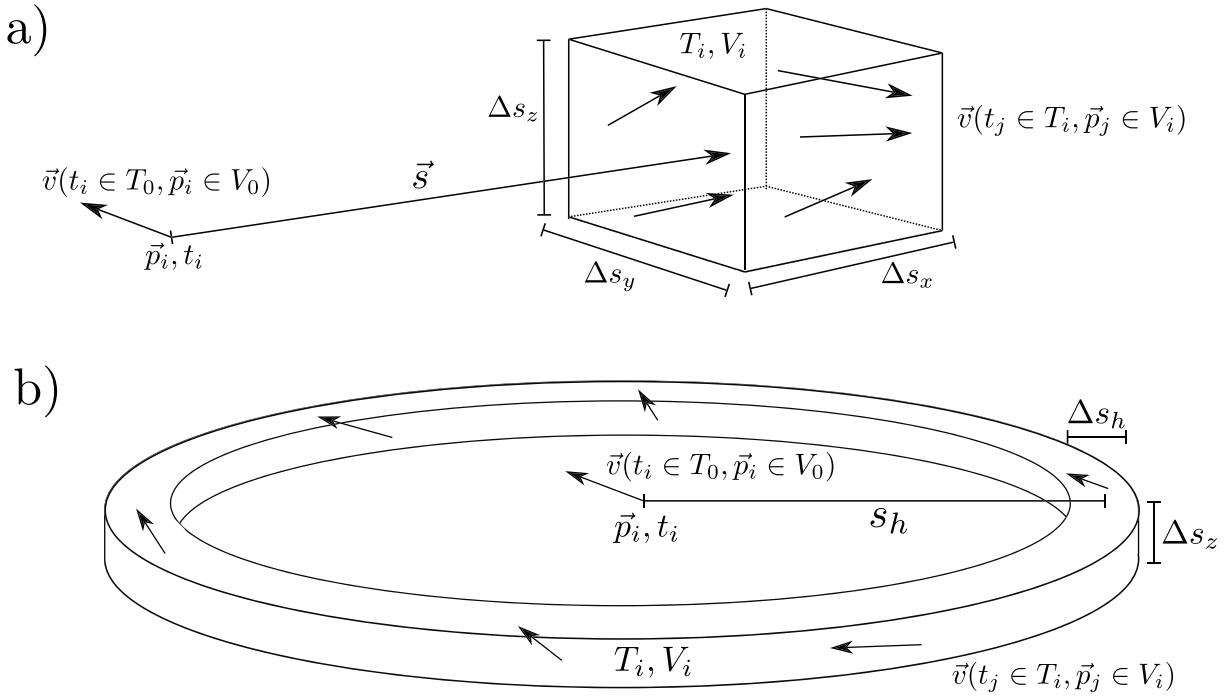
Figure 3. Selection of lagged-product measurements. There are two four-dimensional sets, which are used to constrain measurements in space and time. The first set determines what region of space-time is being the correlation function estimated in $t_i \in T_0$, $\vec{p}_i \in V_0$. The first measurement of a lag-product measurement m_{ij} is selected from this set. The second set $t_j \in T_i$, and $\vec{p}_j \in V_i$ depends on the position and time of the first measurement and is determined by the lag and the lag resolution of the lag-product measurement. Two different cases are shown. (a) The spatial lag is $\vec{s}$ and the lag resolution is Δs_x, Δs_y, and Δs_z. (b) The spatial lag is specified with horizontal length s_h, horizontal lag resolution Δs_h, and vertical resolution Δs_z.

$$= \langle u_\alpha(t,\vec{p})^2 \rangle + \langle u_\beta(t',\vec{p}')^2 \rangle - 2\langle u_\alpha(t,\vec{p})u_\beta(t',\vec{p}') \rangle. \tag{31}$$

The first two terms are zero lags of the correlation function: $\langle u_\alpha(t,\vec{p})^2 \rangle = G_{\alpha\alpha}(0,0)$ and $\langle u_\beta(t',\vec{p}')^2 \rangle = G_{\beta\beta}(0,0)$. The last term is the cross-correlation term with a lag: $\langle u_\alpha(t,\vec{p})u_\beta(t',\vec{p}') \rangle = G_{\alpha\beta}(t - t', \vec{p} - \vec{p}') = G_{\alpha\beta}(\tau,\vec{s})$. It is therefore possible to relate the structure function to the correlation function as follows:

$$S_{\alpha\beta}(\tau,\vec{s}) = G_{\alpha\alpha}(0,0) + G_{\beta\beta}(0,0) - 2G_{\alpha\beta}(\tau,\vec{s}). \tag{32}$$

When comparing the same component α of the wind, this becomes

$$S_{\alpha\alpha}(\tau,\vec{s}) = 2G_{\alpha\alpha}(0,0) - 2G_{\alpha\alpha}(\tau,\vec{s}). \tag{33}$$

The structure function can therefore be estimated from the correlation function.

The structure function is useful since it is less sensitive to low-frequency components than the correlation functions. Moreover, it can be directly compared with outputs from models predicting a power law kinetic energy spectrum, such as Kolmokorov (Kolmogorov, 1941). This can be done in lag-domain without Fourier transforming the correlation function estimate. If the spectral shape has a power law form $|k|^{-p}$, the structure function also has a power law form: $S_{\alpha\alpha}(\tau) = \alpha|\tau|^{p-1}$ when $1 < p < 3$ (e.g., Yaglom, 1952).

2.9. Spectral Representation

The Wiener-Khinchin theorem relates correlation functions (autocorrelation and cross-correlation functions) to power and cross-power spectra via a Fourier transform relationship. For example, it is possible to Fourier transform the temporal correlation function, $G_{\alpha\beta}(\tau,0)$ as follows:

$$\hat{G}_{\alpha\beta}(\omega_\tau) = 2\int_0^\infty G_{\alpha\beta}(\tau,0)e^{-i\omega_\tau \tau}d\tau \tag{34}$$

to obtain the power spectrum of wind velocity fluctuations on various timescales. Analogously, one can Fourier transform a one-dimensional spatial correlation function ($G_{\alpha\beta}(0, s)$):

$$\hat{G}_{\alpha\beta}(\omega_s) = 2 \int_0^\infty G_{\alpha\beta}(0, s)e^{-i\omega_s s}\mathrm{d}s. \tag{35}$$

Multidimensional Fourier transforms of the joint time and spatial lag correlation functions could also be estimated, that is, multidimensional cross-power spectra ($\hat{G}_{\alpha\beta}(\omega_\tau, \omega_s)$).

2.10. Kinetic Energy

The mean magnitude squared of the wind velocity vector is related to the zero-lag of correlation function as follows:

$$\langle|\vec{v}_n(0,0)|^2\rangle = G_{uu}(0, 0) + G_{vv}(0, 0) + G_{ww}(0, 0). \tag{36}$$

The kinetic energy density of a parcel of air that is measured would thus be given by

$$E = \frac{1}{2}\rho \left(G_{uu}(0, 0) + G_{vv}(0, 0) + G_{ww}(0, 0) \right) \ (\mathrm{J/m^3}), \tag{37}$$

where ρ is air mass density. By varying the size of a volume that is being inspected, it is possible to study the kinetic energy density of the wind field at different scale sizes.

The spatial and temporal lags on the other hand provide information on how the wind field kinetic energy is correlated in time and space. For example, a temporal correlation function for a monochromatic wave will be a sinusoid. Turbulence on the other hand is a stochastic process and will cause the wind to decorrelate as a function of time and space and the correlation will approach zero for a long enough lag in space and time. The length scale of this decorrelation tells us about the integral scale of turbulence.

3. Results

In this section, we present results of our correlation function estimation methodology using measurements obtained during a recent 7-day multistatic SMR campaign called Spread-spectrum Interferometric Multistatic meteor radar Observing Network 2018. The goal of this campaign was to study the spatial and temporal structure of the mesospheric wind with a large number of specular meteor echoes. For this study, we have used 24 hr of measurements (5 November 2018 00:00 to 24:00 UTC) obtained during the campaign. The main intent of this study is to introduce and demonstrate the new correlation function estimation method. The results from the full campaign are planned to be presented in subsequent studies.

The radar network used in the campaign consisted of two pulsed transmitters in Juliusruh and Collm (e.g., Stober et al., 2018). Six receiver stations were used forming two monostatic and four bistatic links to receive radar echoes from the pulsed transmitters. We also used a new coded MIMO continuous-wave (MIMO-CW) transmitter developed in-house. The MIMO-CW transmitter used five interferometric transmit antennas located in Kühlungsborn. Six bistatic receive stations located in Mechelsdorf, Breege, Neustrelitz, Guderup, Salzwedel, and Bornim were used to receive echoes. The details of the MIMO-CW system are described in Vierinen et al. (2016) and Chau et al. (2019). The locations of all transmitters and receivers, and meteor detections during a 24-hr interval are shown in Figure 4.

During this campaign, we observed approximately $2 \cdot 10^5$ meteors per day using the whole radar network. Out of all meteors, we filtered out approximately 10^5 high-quality meteor detections. The selection criterion was that the detections should be within 3 standard deviations of the MWE fit residuals. We also required that the detections should be more than 30° above the horizon, to ensure that good interferometric angle of arrival estimates can be obtained (Chau et al., 2019).

We have previously tested the accuracy of meteor position estimates using the MIMO radar technique (Chau et al., 2019), which allows observing the locations of the same meteor with two independent determinations: transmit and receive interferometry. This has allowed us to characterize the position accuracy of meteor detections. We know that the locations of the detected meteors should on average have about 5-km uncertainties in horizontal location. The interferometry phases of the MIMO-CW links were calibrated using
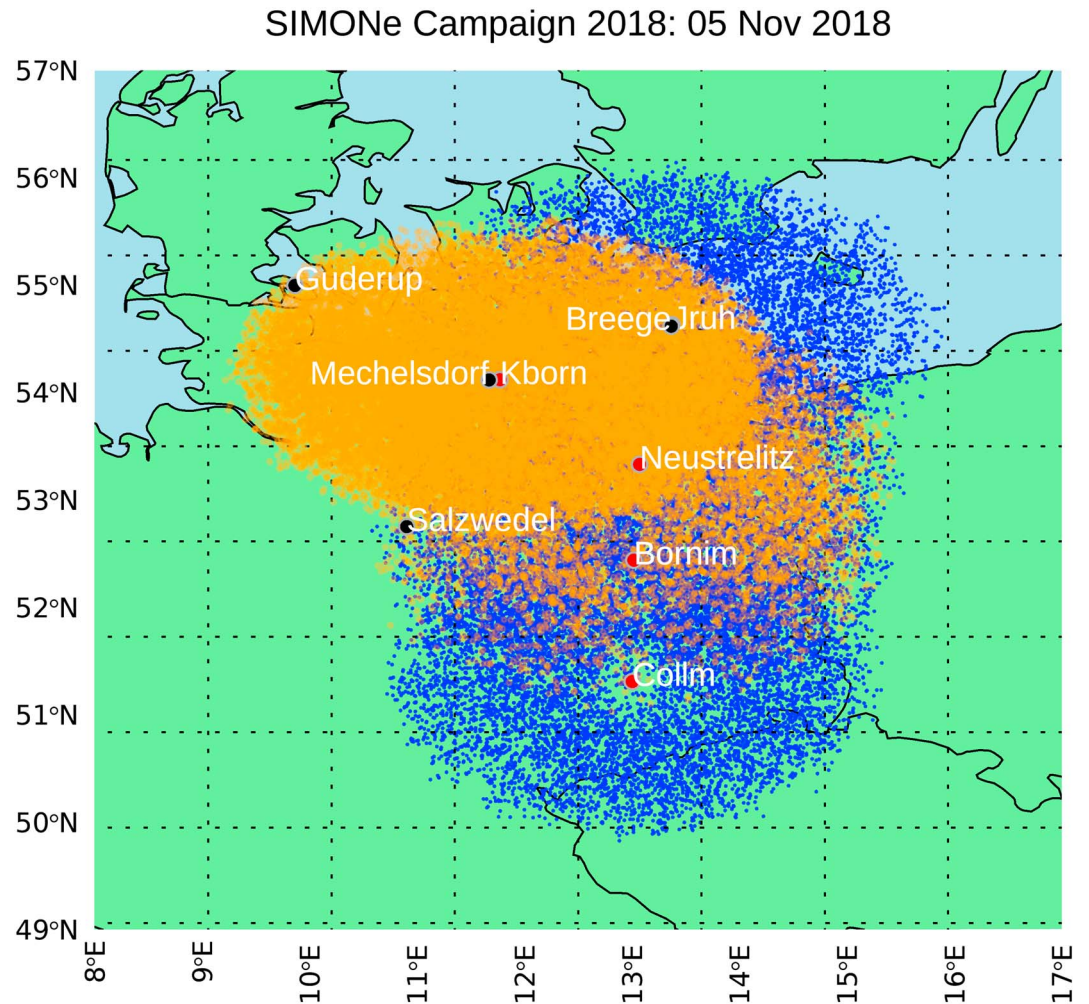
Figure 4. Locations of transmit and receive stations operated during the Spread-spectrum Interferometric Multistatic meteor radar Observing Network (SIMONe) 2018 campaign. Positions of meteor detections during a 24-hr interval are shown in blue for the links using the pulsed transmissions and in orange those from the multi-output and multi-input continuous-wave transmissions. Grid dotted lines represent 100-km distances at 90-km altitude. Only filtered detections are shown. See text for more details.

the beamforming approach of Chau and Clahsen (2019). All of the stations were synchronized to a Global Positioning Service-stabilized reference oscillator, so each detection time was accurate to less tjam 1 µs.

3.1. Measurement Pairs

With the 10^5 measurements that were obtained in 24 hr, it is possible to form $5 \cdot 10^9$ unique combinations of pairs. In order to demonstrate how these pairs of measurements are displaced in space and time, we have computed two-dimensional histograms of the horizontal and temporal displacements for pairs of meteors that are within 1 km of each other in altitude. Two-dimensional histograms for four different altitude ranges are shown in Figure 5.

While most measurements are spaced relatively far apart, there are also quite many pairs of measurements with very small displacements. There are many combinations of measurements with <10 km difference in horizontal distance and <100-s distance in time, which should in theory allow observing waves periods close to Brunt-Väisälä period, as well as to obtain spatial structure of wind fluctuations down to 10 km in the horizontal direction. Such measurements will allow us to obtain high resolution information about the wind field correlation function. The longer spacings are also useful, as they provide information about larger scale correlations within the wind field.
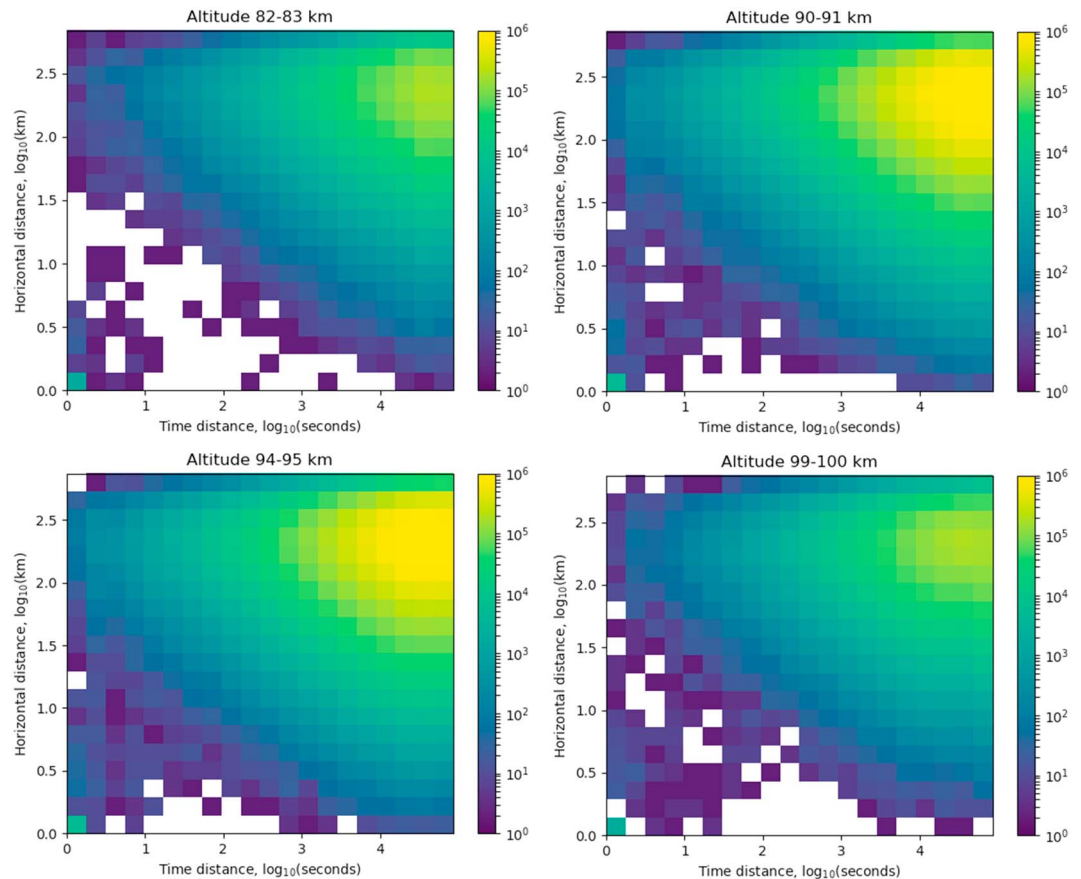
Figure 5. Two-dimensional histograms of horizontal and temporal displacements of measurement pairs, which are within 1 km of each other in the vertical direction, estimated at four different altitude ranges: (a) 83–84, (b) 90–91, (c) 94–95, and (d) 99–100 km. We have also included self-correlation pairs (zero-lag) measurement in this histogram.
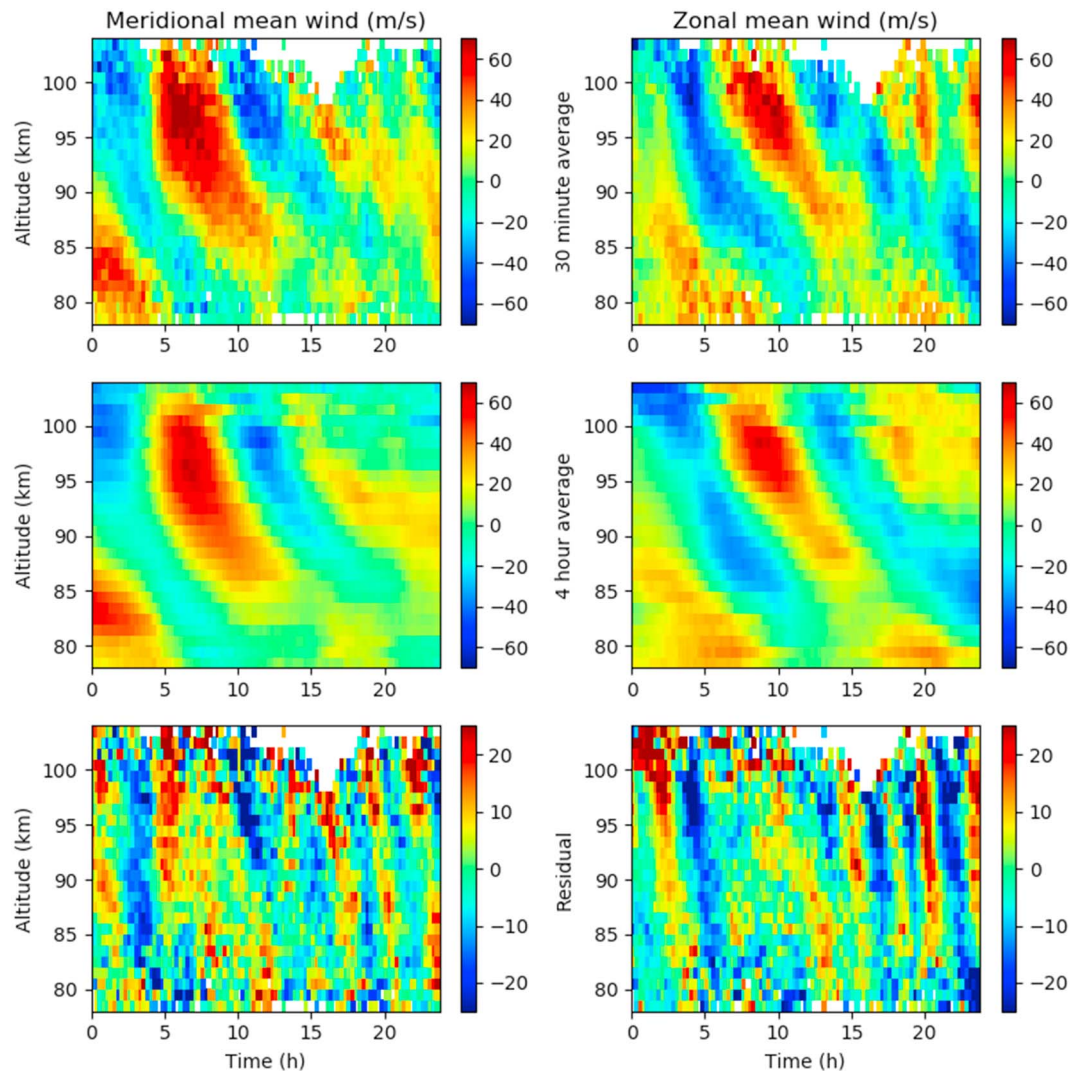
3.2. Mean Horizontal Wind

The mean horizontal winds estimated from the measurements with the MWE method are shown in Figure 6. We have estimated the winds with two time resolutions: 30 min and 4 hr (the top and middle panels). The 4-hr mean wind was subtracted from the 30-min mean wind to get an idea on waves with periods larger than 30 min and smaller than 4 hr. The wind residuals are shown in the bottom rows of the plot. The mean winds show a typical behavior for mesospheric winds. One can clearly see tidal modes, but also hints of higher-frequency waves.

The residuals of the 4-hr mean wind clearly show a quasi 3-hr wave both in the zonal and meridional wind velocity components. For the 3-hr wave, the vertical wavelength is large (at least more than 30 km) between 2000 and 2300 UTC. Using gravity wave linear theory for high-frequency waves the expected horizontal wavelength would be at least 1,300 km (e.g., Fritts & Alexander, 2003). Three-hour waves in the winter mesosphere at polar latitudes have been reported by Rapp et al. (2011). In their case the estimated horizontal wavelength was about 500 km, given that the vertical wavelength was ~10 km. Given that in our case the vertical and horizontal wavelengths are much larger, these 3-hr waves might be due to secondary gravity waves that are expected to occur in the winter mesosphere (e.g., Vadas & Becker, 2018).

3.3. Mean Horizontal Wind Comparison

In order to validate our WCFI method, we have compared it with the MWE method. Finding that results obtained with two methodologies do match would suggest that our WCFI method is likely to work as well as with higher spatial and temporal resolutions, at which the mean wind field estimation cannot be done due to insufficient number of simultaneous measurements.

The MWE method described in section 2.5 provides an estimate of $\bar{u}$ and $\bar{v}$ on large spatial and temporal scales. The mean horizontal wind obtained with the MWE method is shown in 6. The mean horizontal wind
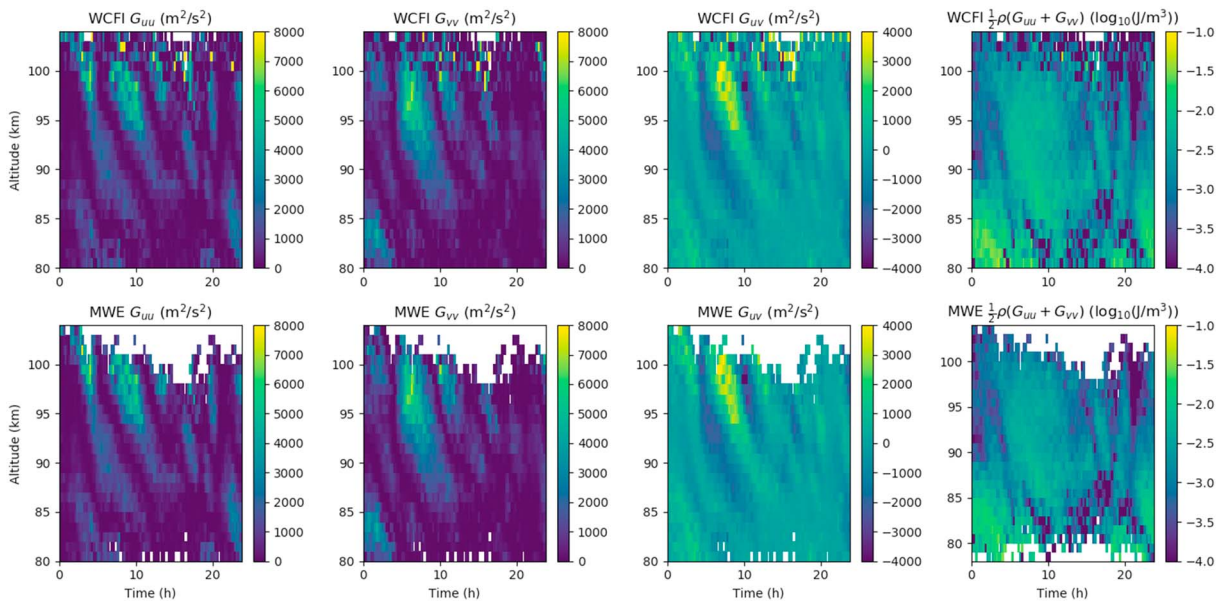
Figure 6. Mean horizontal winds estimated using the standard method (mean wind estimation). On the top row, the time resolution is 30 min. The middle row shows a 4-hr average, and the bottom row shows the residuals when the 4-hr mean is subtracted from the 30-min mean wind. It is possible to see a quasi 3-hr wave in the residuals with a relatively steep altitude slope.

estimate can be directly used to estimate the zero-lag of the large scale correlation function $\bar{G}_{uu}(0,0) = \bar{u}^2$, $\bar{G}_{vv}(0,0) = \bar{v}^2$, and $\bar{G}_{uv}(0,0) = \bar{u}\bar{v}$.

With the WCFI method, as described in section 2.4, one can also estimate these same quantities, by assuming that the correlation function is constant for an altitude and time bin, independent of horizontal location. In order to estimate the mean correlation function, we have used the same time and altitude binning as we used for the 30-min MWE, which provides us with the same time and altitude resolution.

The top panels of Figure 7 shows the mean horizontal correlation function calculated using the WCFI method by cross-correlating pairs of measured Doppler velocities. We have not used zero-lag measurements (m_{ii}) to avoid estimation bias. The bottom panels of the same Figure shows the same correlation function estimated from the 30-min mean wind estimates obtained with the MWE method. Both methods produce similar correlation functions with similar features.

The right-hand side panels of Figure 7 also shows the kinetic energy $\frac{1}{2}\rho[\bar{G}_{uu}(0,0)+\bar{G}_{vv}(0,0)]$ of the horizontal mean wind estimated using both methods. The neutral density ρ is obtained from the Mass Spectrometer Incoherent Scatter Radar (MSIS-E-90) model (Bilitza & Papitashvili, 2002). One interesting feature is that the night time kinetic energy shows strong periodic fluctuations, which are consistent with the 3-hr period wave.

Figure 7. Left three panels: zero-lag estimates of the mean wind field correlation function, that is, $\bar{G}_{uu}(0,0)$, $\bar{G}_{vv}(0,0)$, and $\bar{G}_{uv}(0,0)$ for different times of day and altitude. Right-hand side panels: kinetic energy of the mean horizontal wind $\frac{1}{2}\rho(\bar{G}_{uu}(0,0) + \bar{G}_{vv}(0,0))$. Half-hour average are used to form the estimates. The top row shows the estimates derived using the WCFI method, and the bottom row shows the same correlation function estimated from the mean horizontal wind estimate shown in Figure 6. WCFI = wind field correlation function inversion; MWE = mean wind estimation.

Figure 8 shows scatter plots of the mean wind correlation function estimates obtained using the two different methods. There is a very good agreement for all of the three estimated quantities, which indicates that the WCFI method works as expected. One notable feature is that the mean correlation function obtained from the MWE method is slightly biased toward a higher value for very low values of the correlation function. This is to be expected due to correlated estimation errors of the mean wind. Neither of the methods shows a significant bias for the cross-correlation $\bar{G}_{uv}(0,0)$, because the MWE errors are not correlated for either of the methods.

3.4. Temporal Correlations and Frequency Spectra

One advantage of the WCFI method lies in possibility of obtaining high spatial and temporal resolution information on the wind field statistical properties. As long as sufficient number of lagged-product
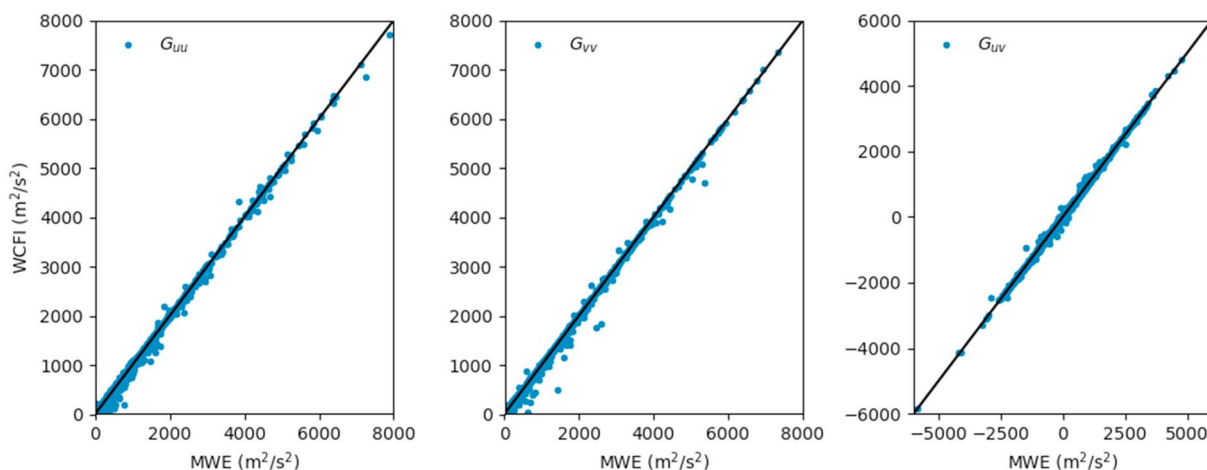
Figure 8. Scatter plots comparing the 2,400 horizontal correlation function estimates obtained using the WCFI and MWE methods. The same measurements are shown in Figure 7. The two methods agree well with one another. The main difference is that the MWE method is slightly biased for very low values of $G_{uu}(0,0)$ and $G_{vv}(0,0)$, due to correlated measurement errors in the mean wind estimates. Note that the cross-correlation estimates $G_{uv}(0,0)$ are unbiased in both methods. WCFI = wind field correlation function inversion; MWE = mean wind estimation.

Table 1
Selection Criteria for Lagged-Product Measurement Pairs When Estimating the Temporal Autocorrelation Functions, Which Are Shown in Figure 9

Name	Symbol	Time resolution $\Delta\tau$ (s)	Altitude resolution Δs_z (km)	Horizontal resolution Δs_h (km)
Large scale	$\bar{G}_{\alpha\alpha}(\tau,0)$	900	1	500
Small scale	$G_{\alpha\alpha}(\tau,0)$	900	1	100
Fluctuating <4 hr	$G\alpha\alpha, 4h'(\tau,0)$	900	1	100
Fluctuating <1 hr	$G\alpha\alpha, 1h'(\tau,0)$	200	1	100

measurements can be obtained with a certain range of desired temporal and spatial displacements, the correlation function of the wind field can be estimated at this lag. This means that we do not rely on being able to measure everything at once but can slowly build up a high resolution estimate over time.

As an example of the type of temporal information one can get, we have obtained temporal autocorrelation function estimates with lags τ between 0 and 12 hr. We have estimated four different correlation functions: $\bar{G}_{\alpha\alpha}(\tau,0)$, $G_{\alpha\alpha}(\tau,0)$, $G'_{\alpha\alpha,4h}(\tau,0)$, and $G\alpha\alpha, 1h'(\tau,0)$. Each of these have different selection criteria, which is explained in the following paragraphs.

In order to estimate the temporal structure of the large horizontal scale mean wind $\bar{G}_{\alpha\alpha}(\tau,0)$, we allowed horizontal displacements of up to $\Delta s_h = 500$ km, and temporal displacements of $\Delta\tau = 900$ s. We also estimated a correlation function $G_{\alpha\alpha}(\tau,0)$, which contains contributions from the mean wind and smaller horizontal scale fluctuating wind. The only difference to $\bar{G}_{\alpha\alpha}(\tau,0)$ was that we used a horizontal lag resolution of $\Delta s_h = 100$ km. Two temporal correlation functions representative of short period waves, were estimated with high-pass-filtered measurements by subtracting 4- and 1-hr mean winds from the Doppler measurements before using the WCFI to obtain $G\alpha\alpha, 4h'(\tau,0)$ and $G\alpha\alpha, 1h'(\tau,0)$, respectively. The last two estimates were obtained with a horizontal resolution of $\Delta s_h = 100$ km. The temporal lag resolution for $G\alpha\alpha, 4h'(\tau,0)$ was $\Delta\tau = 900$ s and for $G\alpha\alpha, 1h'(\tau,0)$ $\Delta\tau = 200$ s. In all cases, the mean horizontal and vertical lags were 0 ($s_h = s_z = 0$). The vertical lag resolution for all cases was $\Delta s_z = 1$ km. All measurements observed during the 24 hr between 92 and 95 km were averaged together using weighting to ensure even weighting across all times of day. The selection criteria for the lagged-product measurements for the four different correlation function estimates are shown in Table 1.

The estimated temporal autocorrelation functions for the horizontal wind components are shown in Figure 9. The top left plot shows the 500-km horizontal scale autocorrelation function $\bar{G}_{\alpha\alpha}(\tau,0)$ and the 100-km scale autocorrelation function $G_{\alpha\alpha}(\tau,0)$. Note that $\bar{G}_{\alpha\alpha}(\tau,0)$ is almost completely dominated by the 12-hr tide. The 100-km horizontal scale autocorrelation function $G_{\alpha\alpha}(\tau,0)$ deviates from $\bar{G}_{\alpha\alpha}(\tau,0)$ only at short temporal lags, where small spatial scale waves are also present. These waves do not correlate over longer periods of time.

The center left panel of the plot shows high-pass-filtered correlation functions $G'_{\alpha\alpha,4h}(\tau,0)$ and the bottom left plot of the Figure shows high-pass-filtered correlation function estimates $G'_{\alpha\alpha,1h}(\tau,0)$. From $G'_{\alpha\alpha,4h}(\tau,0)$, it is possible to see a damped sinusoidal form, which has approximately as 3-hr period. For the <1-hr fluctuating component $G'_{\alpha\alpha,1h}(\tau,0)$, the correlation gradually decreases to zero at the 3,600-s lag. No clear oscillations are seen in this correlation function.

Just using 24 hr of data, it is possible get some idea of the partitioning of energy into different wave periods. The full-correlation function shows that the maximum value of $G_{uu}(0,0)$ and $G_{vv}(0,0)$ within the zero lag is about 850 and 1,100 m^2/s^2. The mean tidal mode wind at a 12-hr lag $\bar{G}_{uu}(12h,0)$ and $\bar{G}_{vv}(12h,0)$ is about 500 and 750 m^2/s^2. The fluctuating sub-4-hr peaks at $G'_{uu,4h}(0,0)$ and $G'_{vv,4h}(0,0)$ are 280 and 200 m^2/s^2, and finally, the sub-1-hr fluctuating components $G'_{uu,1h}(0,0)$ and $G'_{vv,1h}(0,0)$ peak at 80 and 100 m^2/s^2. The 3-hr wave mode has about 100- and 50-m^2/s^2 amplitudes for u and v components, respectively. From this, one can deduce that (a) 60–70% of the kinetic energy in the horizontal wind is within the semidiurnal tides, (b) 20–30% is within the sub-4-hr fluctuations, (c) 10% of the energy of the zonal wind is within the 3-hr wave, (d) about 5% of the energy of the meridional wind is within the 3-hr wave, and (e) about 10% of the horizontal wind energy is within the sub-1-hr fluctuations. Obtaining statistically significant values would
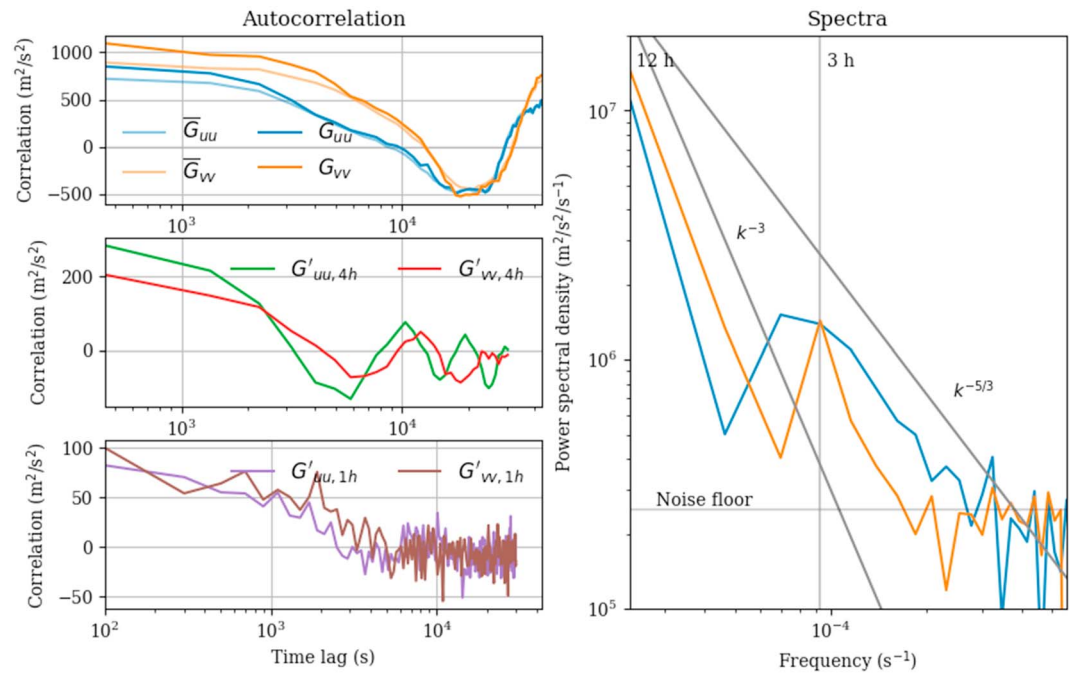
Figure 9. Temporal autocorrelation functions of the horizontal wind up to 12-hr temporal lags, averaged for heights from 92 to 95 km over 24 hr. Top left: The mean $\bar{G}_{\alpha\alpha}(\tau, 0)$ and full $G_{\alpha\alpha}(\tau, 0)$ autocorrelation functions evaluated with 900-s time resolution. The horizontal resolution of the full-correlation function is 100 km, whereas for the mean correlation function it is the whole observation region (about 500 km). Center left: high-pass-filtered correlation function $G'_{\alpha\alpha,4h}(\tau, 0)$ evaluated with 900-s time resolution and 100-km horizontal extent. Bottom left: high-pass-filtered correlation function $G'_{\alpha\alpha,1h}(\tau, 0)$ evaluated with 200-s time resolution and 100-km spatial extent. Right: spectrum calculated from the full autocorrelation functions G_{uu} and G_{vv} shown on the top left. No windowing or zero padding is used to calculate the spectra. See text for more details.

require a data set averaged over a significantly longer period of time, as these numbers are only based on 1 day of measurements.

The right-hand panel of Figure 9 shows the power spectra derived from the autocorrelation functions using a fast Fourier transform. We have not used windowing or zero padding in making the spectrum estimate. There is a clear transition from ω^{-3} to $\omega^{-5/3}$ shown on this plot. The transition takes place at about 3 hr, suggesting that there is a mesoscale regime below this threshold. This observation is reinforced by the fact that the 3-hr wave has amplitudes equal to the kinetic energies obtained from the Kühlungsborn Mechanistic general Circulation Model simulations for the gravity waves in a mesoscale regime. The partitioning of energy between 3-hr wave and the sub-1-hr fluctuation component indicates that there is a forward energy cascade at this scale and that the theory of strongly stratified turbulence could be used for further theoretical analysis of turbulence in the winter mesosphere.

From $\bar{G}(\tau, 0)$ and $G4h'(\tau, 0)$, it is possible to see a strong peak around 3-hr wave periods—this is consistent with the mean wind residuals shown in Figure 6 and the oscillations that can be seen in the corresponding autocorrelation function. Sato et al. (2017) also report the presence of a 3-hr wave. Our spectra only contains 1 day of measurements, so the fidelity is not as good. The 3-hr wave might be due to secondary gravity waves with large vertical (>30 km) and horizontal (>1,300 km) wavelengths occurring between 2000 and 2300 UT.

The results are still too noisy to make a high-quality spectrum estimate for wave periods less than about 1 hr. Waves with periods shorter than 1 hr are mostly measurement noise in the spectrum, because of estimation uncertainties in the correlation functions. We also do not show any cross-correlation terms, even though they were estimated. These terms are small in magnitude and with only a 24-hr data set, they are too noisy to be reliably estimated. The uncertainties originate mainly from two sources: Doppler velocity measurement uncertainties, and self-noise due to the stochastic nature of the wind field itself. The latter can have long correlation times, which necessitates longer data set than 24 hr in order to reduce the errors. For example, we
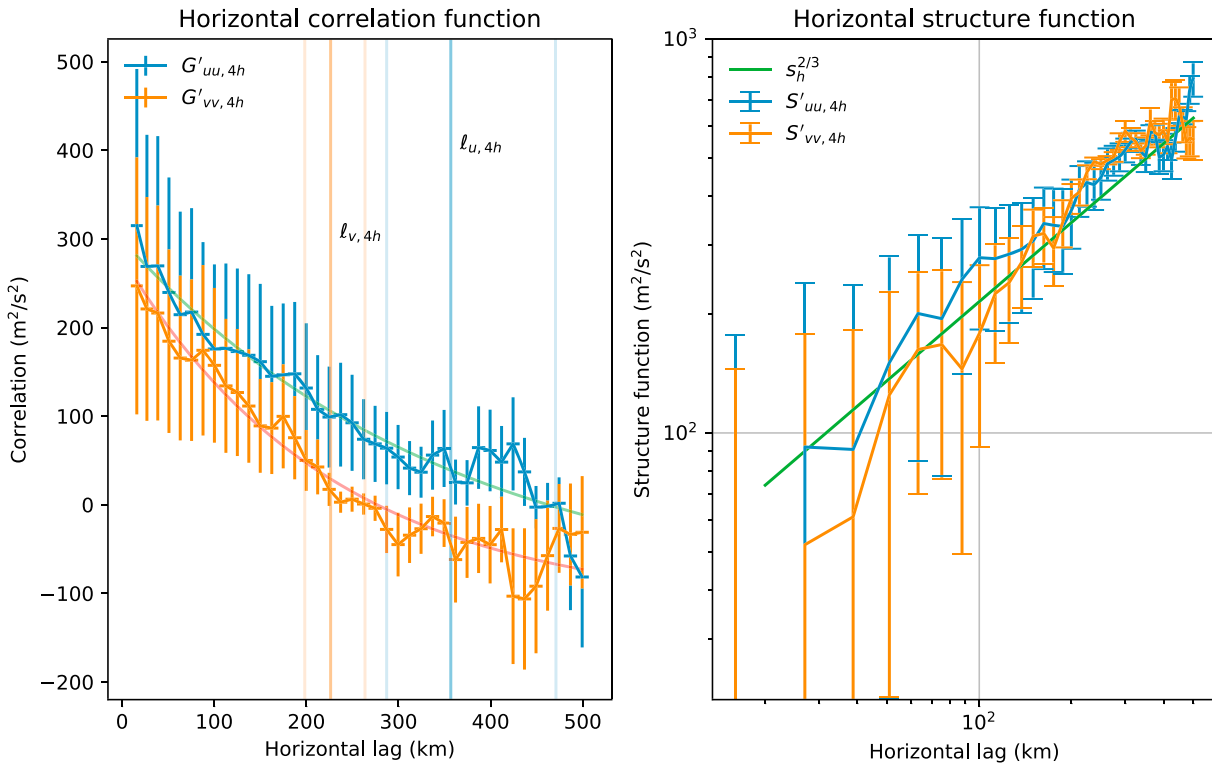
Figure 10. Left: Horizontal correlation function for the <4-hr fluctuating components of the horizontal wind $Guu, 4h'(0, s_h)$ (blue) and $Gvv, 4h'(0, s_h)$ (orange) as a function of horizontal displacement, averaged from 92 to 95 km. We have used a $\Delta s_h = 25$ km spatial lag resolution and 900-s temporal lag resolution ($\Delta\tau = 900$ s) for the lagged-product measurements used to estimate the correlation function. An exponential function fit to the correlation function is shown in green (Guu') and red (Gvv'). The e-folding lengths corresponding to these fits, $\ell_{u,4h}$ and $\ell_{v,4h}$, are shown with vertical lines with the 1σ confidence interval shown with the lighter color. Right: The structure functions of the horizontal wind $Suu, 4h'(0, s_h)$ and $Svv, 4h'(0, s_h)$ derived from the correlation functions. With a green line we show a $s_h^{2/3}$ line, that corresponds to the $k_h^{-5/3}$ horizontal frequency spectrum. .

only observe two periods of the 12-hr wave, which is not enough to capture the long-term average behavior of this wave mode. The same applies also to lesser extent to the shorter period waves.

3.5. Horizontal Spatial Correlations

One outstanding problem in studies of mesospheric dynamics is measuring the spatial correlation function of the mesospheric fluid for a wide range of spatial scales (Roberts & Larsen, 2014). The WCFI method can also be applied to obtain information about the spatial correlations of the wind at scales that are difficult to observe otherwise. Multistatic SMRs are ideal tools for observing spatial scales between a few kilometers and several hundred kilometers, with a diversity of Bragg scattering wave vectors. At these scales, waves due to stratified turbulence are expected to coexist with gravity waves, but with different scales in the vertical direction.

We estimated the spatial correlation function of the wind velocity components at horizontal separation s_h lags between 0 and 500 km with horizontal spatial lag resolution of $\Delta s_h = 25$ km. The temporal and vertical lag resolutions were $\Delta\tau = 900$ s, and $\Delta s_z = 1$ km, respectively. We estimated the horizontal correlation functions of the high-pass-filtered fluctuating components of the wind $Guu, 4h'(0, s_h)$ and $Gvv, 4h'(0, s_h)$ with mean 4-hr wind subtracted from the measurements, as described in section 2.3. We use a one-dimensional horizontal distance s_h as the lag variable, which indicates displacement only in the horizontal direction. We averaged the pairs of measurements that satisfied these criteria over 24 hr of observations and altitudes between 92 and 95 km. We used weighting, as described in section 2.2, to ensure that all times of day had equal contribution to the horizontal correlation function.

The estimated spatial correlation functions are shown on the left panel of Figure 10. From this plot, one can observe that the fluctuating wind gradually decorrelates as a function of horizontal displacement, as is to be expected. While we estimated all six correlation functions, we only show the two spatial autocorrelations of

the horizontal wind components, as the other terms are small in magnitude and too noisy to provide useful information with the 24-hr data set used in this work.

To estimate the length scale after which the field is decorrelated, we have fit an exponential function $f(s_h) = a_0 e^{-\kappa |s_h|}$ to the meridional and zonal spatial autocorrelation functions. This allows us to estimate the e-folding horizontal length scale $\ell = 1/\kappa$ of the fluctuating wind energy. For the zonal component of the wind, the e-folding distance is $\ell_{u,4h} = 357[+184, -114]$ km. For the meridional wind component it is $\ell_{v,4h} = 226[+65, -37]$ km. We have estimated the e-folding distance with several different structure functions with different temporal high-pass filter cutoffs and find that the e-folding length scale seems to depend on the high-pass filter cutoff period. For shorter period waves, this cutoff is shorter than for longer period waves. For the sub-1-hr high-pass-filtered fluctuating component, the horizontal e-folding scale length is about 100 km, and for the sub-half-hour high-pass-filtered fluctuating component it is about 70 km. However, providing a reliable characterization of length scales as a function of temporal scale is not possible without a larger data set, due to measurement uncertainties. Characterizing the horizontal length scales for different temporal scales is a topic of future work.

In order to estimate the horizontal spatial frequency spectral index, we estimated the structure functions $Suu, 4h'(0, s_h)$ and $Svv, 4h'(0, s_h)$ from the correlation functions, as discussed in section 2.8. The structure function is shown on the right-hand side of Figure 10 on a log-log scale. For a Kolmogorov $k_h^{-5/3}$ spectral shape (Kolmogorov, 1941), one would expect the structure function to follow a $s_h^{2/3}$ power law. We have overlayed this on top of the plot. The $s_h^{2/3}$ power law approximately follows the structure function, indicating that the Kolmogorov $-5/3$ spectral power law also applies to horizontal spatial scales at these timescales. This indicates that for sub 4-hr waves, the horizontal wind fluctuations change their slope from -3 to $-5/3$ spectral slope. At horizontal scales of a several hundred of kilometers, we expect to see a joint spectrum of mesoscale gravity waves and strongly stratified turbulent structures. Presently, it is impossible to quantify if waves or vortical modes are dominating the spectrum at these horizontal scales, as both types of motions share the same $-5/3$ spectral slope. The question of separation of these two modes will be addressed in the future studies.

3.6. Vertical Correlation Function
The last example of the use of the WCFI method is a study of vertical structure. The vertical structure function is interesting, because gravity waves break in the mesosphere and deposit horizontal momentum. Also, different theories of gravity waves and stratified turbulence predict different vertical scales for short period fluctuations.

In order to estimate the vertical scale length of short period waves, we have estimated the correlation function $G1h'(0, s_z)$ of the sub-1-hr fluctuating component of the wind field. We are now using a one-dimensional spatial lag s_z, which indicates displacement only in the vertical direction. The measurements are high-pass filtered with a 1-hr mean horizontal wind estimate before correlation function estimation. We used 1-km lags s_z in the vertical direction and with zero-mean horizontal and temporal lags ($s_h = \tau = 0$). The pairs of measurements were selected corresponding to a horizontal lag resolution of $\Delta s_h = 100$ km and temporal lag resolution of $\Delta \tau = 600$ s. The correlation function was averaged over the 24-hr measurement period, using weighting to ensure the estimate has even contribution for each time of day. One altitude was used as the reference altitude, and we estimated vertical lags s_z at 1-km displacements above and below the reference altitude separately, as positive and negative lags are expected to behave differently.
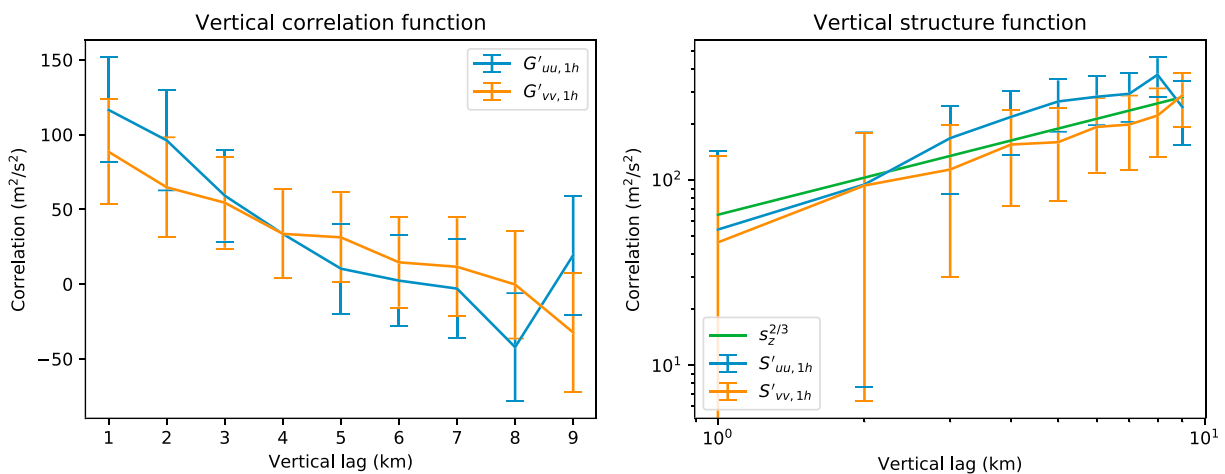
The vertical correlation function of the fluctuating wind for one representative altitude is shown on the left-hand side of Figure 11. We show the uncertainties only at the zero-lag altitude to avoid clutter, as the measurements are very noisy. The vertical correlation function shows a localized peak that is approximately 10 km in vertical extent. Only the zonal and meridional wind components show a significant departure from zero. The behavior is similar at all altitudes that can be estimated between approximately 80 and 100 km. The peak of the correlation function at the zero lag is relatively sharp, which indicates a spectral index <2. In order to study this further, we have plotted positive lags between 0 and 10 km for the two horizontal components. The correlation function, we estimated the corresponding structure functions $Suu, 1h'(0, s_z)$ and $Svv, 1h'(0, s_z)$ and plotted them on a log-log scale to get an idea of the spectral index. These are shown in Figure 12. For a Kolmogorov $k_z^{-5/3}$ spectral distribution of energy, the structure function is expected to
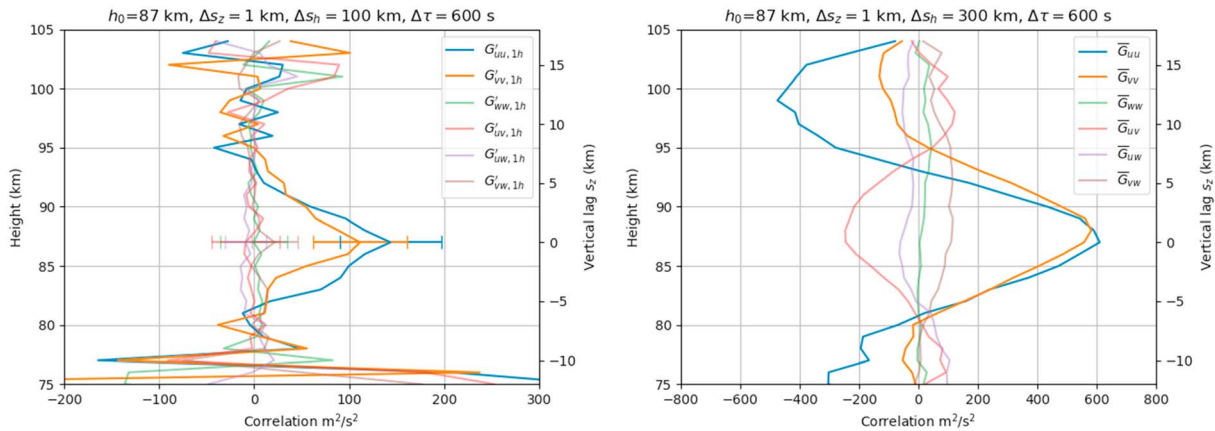
Figure 11. Vertical correlation functions of the mesospheric wind. Left: fluctuating component of the wind field with reference altitude at 87 km. The fluctuating wind correlation function has a sharp peak, which indicates a spectral shape k^{-p} with $1.5 < p < 2$. The length of the peak in horizontal velocity maxima is approximately 10 km. The correlation function estimate is extremely noisy above 95 km and below 80 km due to relatively few measurement pairs at these lags. Right: mean component of the wind, with reference altitude at 87 km. The mean wind vertical correlation function is approximately sinusoidal and has a 14-km (peak to peak) vertical wavelength.

follow a power law of the form $s_z^{2/3}$. The vertical spatial lags approximately follow this shape, although the uncertainties are too large for the result to be statistically significant.

We also estimated the mean wind correlation function $\bar{G}(0, s_z)$ in the vertical direction. We used unfiltered measurements and formed measurement pairs that had less than 300 s of temporal displacement (horizontal lag resolution $\Delta\tau = 600$ s), less than 100-km horizontal displacement (lag resolution $\Delta s_h = 200$ km) and were within 0.5 km of the vertical lag that was being estimated (vertical lag resolution $\Delta s_z = 1$ km). The vertical correlation function of the mean wind for one representative altitude (87 km) is shown on the right-hand side of Figure 11. The vertical correlation function shows a quasi sinusoidal behavior with a vertical wavelength (peak-to-peak) that is roughly 24 km. The horizontal wind terms $\bar{G}_{uu}(0, s_z)$, $\bar{G}_{vv}(s_z)$ appear to be in phase with a similar amplitude. The cross-term $\bar{G}_{uv}(0, s_z)$ is 180° out of phase but has a similar wavelength. The terms including vertical wind $\bar{G}_{ww}(0, s_z)$, $\bar{G}_{uw}(0, s_z)$, and $\bar{G}_{vw}(0, s_z)$ are small in amplitude, but not zero. With only a 24-hr data set, we only measure two periods of the 12-hr tide, which means that it is impossible to estimate error bars for these quantities and to judge if the values are meaningful or not.

Figure 12. Vertical correlation and structure functions of the high-pass-filtered <1-hr fluctuating component of the wind. Only positive lags indicating altitudes above 87 km are used. Left: the vertical autocorrelation functions for the horizontal wind components. Right: The structure function corresponding the correlation function, plotted in log-log scale. The structure function $s_z^{2/3}$ corresponding to the Kolmogorov $k_z^{-5/3}$ spectral shape is shown with a green line.

4. Discussion

In this study, we have shown for the first time high spatiotemporal resolution estimates of the temporal, horizontal, and vertical correlation functions of mesospheric wind obtained using an SMR, allowing us to observe phenomena, such as turbulence and gravity waves. Our main findings from a limited 24-hr data set are

- From the temporal correlation function, we have identified the dominant 12-hr tidal mode, and also a quasi 3-hr wave, which is characterized by large vertical wavelength and horizontal wavelengths. Since these wavelengths are much larger than those expected for primary gravity waves, they might be due to secondary gravity waves (e.g., Vadas et al., 2018). We were also able to estimate how energy is partitioned into different fluctuating wind components of different timescales and reproduce the well-known result that the temporal spectrum approximately follows the $\omega^{-5/3}$ spectral shape (e.g., Chen & Kraichnan, 1989).
- The horizontal spatial autocorrelation functions for <4-hr fluctuating wind was used to estimate the horizontal scale e-folding lengths. We also obtained an estimate of the horizontal structure function for the horizontal wind components. The horizontal structure function agrees with a $s_h^{2/3}$ power law, which corresponds to a $k_h^{-5/3}$ horizontal spectral shape within the range of spatial displacements estimated.
- The vertical correlation function allowed us to estimate the vertical scale length of the horizontal wind fluctuating components of the wind for <1-hr waves. The vertical scale size was found to be approximately 10 km. The vertical structure function for the fluctuating component also shows a $s_z^{2/3}$ power law, that is, a $k_z^{-5/3}$ power law in the vertical spectrum of the horizontal wind fluctuations.

The next logical step could be to compare the measured correlation functions with numerical models of mesospheric wind that evaluate wind velocity $u_\alpha(t, \vec{p})$ in a four-dimensional grid. It should be relatively straightforward to calculate exactly the same correlation function with exactly the same lag resolution and lags from direct numerical simulations able to reproduce the dynamics of the mesosphere without resorting to the use of models for the small scales (e.g., Marino et al., 2015).

Estimation of the mean wind is not required as part of WCFI processing, unless the measurements need to be high-pass filtered. Therefore, the main limiting factors for accuracy and resolution of the correlation function are (1) the number of measurements that can be used, which determines the integration time that is required to form the correlation function estimate; (2) the correlation timescale of the winds, which determines how long of an integration period is needed in order to get sufficiently many independent samples of the wind field stochastic process; and (3) the errors in position for individual meteor trail echoes, which limits the spatial resolution and can cause leakage of horizontal wind power into the vertical wind estimates.

The results shown in this study only utilize observations obtained during a 24-hr time window. While this is sufficient for demonstrating the utility of the method, a larger data set will be needed in order to further reduce the estimation uncertainties and to unleash the full potential of the method. A longer data set would also provide information about planetary waves, which have long wave periods that can extend for weeks. Applying the method described in this study for larger data sets is a topic of future work.

5. Conclusions

We have described a method for estimating the correlation function of a wind field from a set of sparse and incomplete set of measurements consisting of one-dimensional projections of the wind at randomly sampled points in space and time. The correlation function can be used to study the partitioning of kinetic energy within the mesospheric wind field on a broad range of temporal and spatial scales. It can be used also to estimate the second-order structure function of the wind field, which is useful for comparison with models that predict a power law spectral distribution of energy.

The WCFI method was found to be in good agreement with the standard MWE method, when estimating the zero-lag of the correlation function of the mean horizontal wind. This provides some level of confidence that the method should also work for other cases. We also demonstrated the method for high resolution spatiotemporal characteristics of the mesospheric wind, which are not possible with previous techniques.

One of the enabling factors for this study was the use of a large meteor radar network, which provided us with approximately 10 times more detections of meteors than a conventional single station meteor radar would provide. This allowed us to increase the time resolution of the standard mean wind estimate,

allowing us to detect the quasi 3-hr period gravity wave. The larger number of measurements also allows us to more efficiently measure the correlation functions of different spatial and temporal scales. While the WCFI method can be applied also to a single meteor radar, the extent of spatial lags is confined to the field of view of a single system. Using a network of geographically separated meteor radars is the only way to extend this range.

We have so far explored only a small fraction of possible ways the WCFI method can be utilized. In future work, we aim to apply this method to larger data sets for studies of spatial and temporal scales previously not accessible to SMRs. One interesting avenue of future research is the study of multidimensional correlation functions, which include spatial and temporal lags. Such correlation functions can be used to study mean spatiotemporal evolution of different mesospheric wind wave modes, and their derivatives (e.g., divergence and vorticity).

References

Andrioli, V. F., Fritts, D. C., Batista, P. P., & Clemesha, B. R. (2013). Improved analysis of all-sky meteor radar measurements of gravity wave variances and momentum fluxes. *Annales Geophysicae*, *31*(5), 889–908. https://doi.org/10.5194/angeo-31-889-2013

Baumgarten, G., & Fritts, D. C. (2014). Quantifying Kelvin-Helmholtz instability dynamics observed in noctilucent clouds: 1. Methods and observations. *Journal of Geophysical Research: Atmospheres*, *119*, 9324–9337. https://doi.org/10.1002/2014JD021832

Bilitza, D., & Papitashvili, N. (2002). MSIS-E-90 atmosphere model.

Billant, P., & Chomaz, J.-M. (2001). Self-similarity of strongly stratified inviscid flows. *Physics of Fluids*, *13*(6), 1645–1651. https://doi.org/10.1063/1.1369125

Brethouwer, G., Billant, P., Lindborg, E., & Chomaz, J.-M. (2007). Scaling analysis and simulation of strongly stratified turbulent flows. *Journal of Fluid Mechanics*, *585*, 343368. https://doi.org/10.1017/S0022112007006854

Chau, J. L., & Clahsen, M. (2019). Empirical phase calibration for multi-static specular meteor radars using a beam-forming approach. *Radio Science*, *54*, 60–71. https://doi.org/10.1029/2018RS006741

Chau, J. L., Stober, G., Hall, C. M., Tsutsumi, M., Laskar, F. I., & Hoffmann, P. (2017). Polar mesospheric horizontal divergence and relative vorticity measurements using multiple specular meteor radars. *Radio Science*, *52*, 811–828. https://doi.org/10.1002/2016RS006225

Chau, J. L., Urco, J. M., Vierinen, J. P., Volz, R. A., Clahsen, M., Pfeffer, N., & Trautner, J. (2019). Novel specular meteor radar systems using coherent MIMO techniques to study the mesosphere and lower thermosphere. *Atmospheric Measurement Techniques*, *2019*, 1–23. https://doi.org/10.5194/amt-2018-287

Chen, S., & Kraichnan, R. H. (1989). Sweeping decorrelation in isotropic turbulence. *Physics of Fluids A: Fluid Dynamics*, *1*(12), 2019–2024.

de Wit, R. J., Hibbins, R. E., Espy, P. J., Orsolini, Y. J., Limpasuvan, V., & Kinnison, D. E. (2014). Observations of gravity wave forcing of the mesopause region during the January 2013 major Sudden Stratospheric Warming. *Geophysical Research Letters*, *41*, 4745–4752. https://doi.org/10.1002/2014GL060501

Frisch, U. (1995). *Turbulence: The legacy of A. N. Kolmogorov*. Cambridge: Cambridge University Press. https://doi.org/10.1017/CBO9781139170666.004

Fritts, D. C., & Alexander, M. J. (2003). Gravity wave dynamics and effects in the middle atmosphere. *Reviews of Geophysics*, *41*(1), 1003. https://doi.org/10.1029/2001RG000106

Fritts, D. C., Janches, D., Hocking, W. K., Mitchell, N. J., & Taylor, M. J. (2012). Assessment of gravity wave momentum flux measurement capabilities by meteor radars having different transmitter power and antenna configurations. *Journal of Geophysical Research*, *117*, D10108. https://doi.org/10.1029/2011JD017174

Fritts, D. C., Yuan, L., Hitchman, M. H., Coy, L., Kudeki, E., & Woodman, R. F. (1992). Dynamics of the equatorial mesosphere observed using the Jicamarca MST radar during June and August 1987. *Journal of the Atmospheric Sciences*, *49*(24), 2353–2371. https://doi.org/10.1175/1520-0469(1992)049<2353:DOTEMO>2.0.CO;2

Gardner, C. S., Hostetler, C. A., & Franke, S. J. (1993). Gravity wave models for the horizontal wave number spectra of atmospheric velocity and density fluctuations. *Journal of Geophysical Research*, *98*(D1), 1035–1049. https://doi.org/10.1029/92JD02051

Gardner, C. S., & Yang, W. (1998). Measurements of the dynamical cooling rate associated with the vertical transport of heat by dissipating gravity waves in the mesopause region at the Starfire Optical Range, New Mexico. *Journal of Geophysical Research*, *103*(D14), 16,909–16,926. https://doi.org/10.1029/98JD00683

Haurwitz, B., & Fogle, B. (1969). Waveforms in noctilucent clouds. *Deep-Sea Research*, *16*, 85–95.

Hecht, J. H., Liu, A. Z., Walterscheid, R. L., Franke, S. J., Rudy, R. J., Taylor, M. J., & Pautet, P.-D. (2007). Characteristics of short-period wavelike features near 87 km altitude from airglow and lidar observations over Maui. *Journal of Geophysical Research*, *112*, D16101. https://doi.org/10.1029/2006JD008148

Hines, C. O. (1960). Internal atmospheric gravity waves at ionospheric heights. *Canadian Journal of Physics*, *38*(11), 1441–1481. https://doi.org/10.1139/p60-150

Hocking, W. K. (2005). A new approach to momentum flux determinations using SKiYMET meteor radars. *Annales Geophysicae*, *23*(7), 2433–2439.

Hocking, W. K., Fuller, B., & Vandepeer, B. (2001). Real-time determination of meteor-related parameters utilizing modern digital technology. *Journal of Atmospheric and Solar-Terrestrial Physics*, *63*(2), 155–169.

Holdsworth, D. A., Reid, I. M., & Cervera, M. A. (2004). Buckland Park all-sky interferometric meteor radar. *Radio Science*, *39*, RS5009. https://doi.org/10.1029/2003RS003014

Hysell, D. L., Milla, M. A., & Vierinen, J. (2016). A multistatic HF beacon network for ionospheric specification in the Peruvian sector. *Radio Science*, *51*, 392–401. https://doi.org/10.1002/2016RS005951

Kolmogorov, A. N. (1941). The local structure of turbulence in incompressible viscous fluid for very large Reynolds numbers. *Doklady Akademii Nauk SSSR*, *30*, 301–305.

Kozelov, B. V., & Golovchanskaya, I. V. (2006). Scaling of electric field fluctuations associated with the aurora during northward IMF. *Geophysical Research Letters*, *33*, L20109. https://doi.org/10.1029/2006GL027798

Kudeki, E., & Franke, S. J (1998). Statistics of momentum flux estimation. *Journal of Atmospheric and Solar-Terrestrial Physics*, *60*(16), 1549–1553. https://doi.org/10.1016/S1364-6826(98)00104-7

Lindborg, E. (2006). The energy cascade in a strongly stratified fluid. *Journal of Fluid Mechanics*, *550*, 207–242. https://doi.org/10.1017/S0022112005008128

Lindborg, E. (2007). Horizontal wavenumber spectra of vertical vorticity and horizontal divergence in the upper troposphere and lower stratosphere. *Journal of the Atmospheric Sciences*, *64*(3), 1017–1025. https://doi.org/10.1175/JAS3864.1

Lindborg, E., & Cho, J. Y. N. (2001). Horizontal velocity structure functions in the upper troposphere and lower stratosphere: 2. Theoretical considerations. *Journal of Geophysical Research*, *106*(D10), 10,233–10,241. https://doi.org/10.1029/2000JD900815

Lindzen, R. S. (1981). Turbulence and stress owing to gravity wave and tidal breakdown. *Journal of Geophysical Research*, *86*, 9707–9714. https://doi.org/10.1029/JC086iC10p09707

Marino, R., Mininni, P. D., Rosenberg, D. L., & Pouquet, A. (2014). Large-scale anisotropy in stably stratified rotating flows. *Physical Review E*, *90*, 23018. https://doi.org/10.1103/PhysRevE.90.023018

Marino, R., Pouquet, A., & Rosenberg, D. (2015). Resolving the paradox of oceanic large-scale balance and small-scale mixing. *Physical Review Letters*, *114*, 114504. https://doi.org/10.1103/PhysRevLett.114.114504

Marino, R., Rosenberg, D., Herbert, C., & Pouquet, A. (2015). Interplay of waves and eddies in rotating stratified turbulence and the link with kinetic-potential energy partition. *Europhysics Letters*, *112*, 49001. https://doi.org/10.1209/0295-5075/112/49001

Narita, Y., Glassmeier, K.-H., & Motschmann, U. (2011). High-resolution wave number spectrum using multi-point measurements in space: The Multi-point Signal Resonator (MSR) technique. *Annales Geophysicae*, *29*(2), 351–360. https://doi.org/10.5194/angeo-29-351-2011

Nastrom, G. D., & Gage, K. S. (1985). A climatology of atmospheric wavenumber spectra of wind and temperature observed by commercial aircraft. *Journal of the Atmospheric Sciences*, *42*, 950–960.

Nicolls, M. J., Fritts, D. C., Janches, D., & Heinselman, C. J. (2012). Momentum flux determination using the multi-beam poker flat incoherent scatter radar. *Annales Geophysicae*, *30*(6), 945–962. https://doi.org/10.5194/angeo-30-945-2012

Oks, D., Mininni, P. D., Marino, R., & Pouquet, A. (2017). Inverse cascades and resonant triads in rotating and stratified turbulence. *Physics of Fluids*, *29*(11), 111109. https://doi.org/10.1063/1.5001740

Pautet, P.-D., Taylor, M. J., Fritts, D. C., Bossert, K., Williams, B. P., Broutman, D., et al. (2016). Large-amplitude mesospheric response to an orographic wave generated over the Southern Ocean Auckland Islands (50.7°S) during the DEEPWAVE project. *Journal of Geophysical Research: Atmospheres*, *121*, 1431–1441. https://doi.org/10.1002/2015JD024336

Placke, M., Hoffmann, P., Becker, E., Jacobi, C., Singer, W., & Rapp, M. (2011). Gravity wave momentum fluxes in the MLT-Part II: Meteor radar investigations at high and mid-latitudes in comparison with modeling studies. *Journal of Atmospheric and Solar-Terrestrial Physics*, *73*(9), 911–920. Scientific Results from Networked and Multi-instrument studies based on MST Radar https://doi.org/10.1016/j.jastp.2010.05.007

Placke, M., Hoffmann, P., Latteck, R., & Rapp, M. (2015). Gravity wave momentum fluxes from MF and meteor radar measurements in the polar MLT region. *Journal of Geophysical Research: Space Physics*, *120*, 736–750. https://doi.org/10.1002/2014JA020460

Rapp, M., Latteck, R., Stober, G., Hoffmann, P., Singer, W., & Zecha, M. (2011). First three-dimensional observations of polar mesosphere winter echoes: Resolving space-time ambiguity. *Journal of Geophysical Research*, *116*, 11307. https://doi.org/10.1029/2011JA016858

Rhoads, BruceL., & Sukhodolov, A. N. (2004). Spatial and temporal structure of shear layer turbulence at a stream confluence. *Water Resources Research*, *40*, W06304. https://doi.org/10.1029/2003WR002811

Roberts, B. C., & Larsen, M. F. (2014). Structure function analysis of chemical tracer trails in the mesosphere-lower thermosphere region. *Journal of Geophysical Research: Atmospheres*, *119*, 6368–6375. https://doi.org/https://doi.org/10.1002/2013jd020796

Sato, K., Kohma, M., Tsutsumi, M., & Sato, T. (2017). Frequency spectra and vertical profiles of wind fluctuations in the summer Antarctic mesosphere revealed by MST radar observations. *Journal of Geophysical Research: Atmospheres*, *122*, 3–19. https://doi.org/10.1002/2016JD025834

Schulz-DuBois, E. O., & Rehberg, I. (1981). Structure function in lieu of correlation function. *Applied physics*, *24*(4), 323–329.

Stober, G., & Chau, J. (2015). A multistatic and multifrequency novel approach for specular meteor radars to improve wind measurements in the MLT region. *Radio Science*, *50*, 431–442. https://doi.org/10.1002/2014rs005591

Stober, G., Chau, J. L., Vierinen, J., Jacobi, C., & Wilhelm, S. (2018). Retrieving horizontally resolved wind fields using multi-static meteor radar observations. *Atmospheric Measurement Techniques*, *11*(8), 4891–4907.

Stull, R. B. (2012). *An introduction to boundary layer meteorology* (Vol. 13). Dordrecht: Springer Science & Business Media.

Swenson, G. R., Haque, R., Yang, W., & Gardner, C. S. (1999). Momentum and energy fluxes of monochromatic gravity waves observed by an OH imager at Starfire Optical Range, New Mexico. *Journal of Geophysical Research*, *104*, 6067–6080. https://doi.org/10.1029/1998JD200080

Tatarskii, V. I. (1961). *Wave propagation in turbulent medium*. New York: McGraw-Hill Book Co. Inc.

Thorsen, D., Franke, S. J., & Kudeki, E. (1997). A new approach to MF radar interferometry for estimating mean winds and momentum flux. *Radio Science*, *32*(2), 707–726.

Thorsen, D., Franke, S. J., & Kudeki, E. (2000). Statistics of momentum flux estimation using the dual coplanar beam technique. *Geophysical Research Letters*, *27*(19), 3193–3196. https://doi.org/10.1029/1999GL011196

Urco, J. M., Chau, J. L., Milla, M. A., Vierinen, J. P., & Weber, T. (2018). Coherent MIMO to improve aperture synthesis radar imaging of field-aligned irregularities: First results at Jicamarca. *IEEE Transactions on Geoscience and Remote Sensing*, *56*(5), 2980–2990. https://doi.org/10.1109/TGRS.2017.2788425

Urco, J. M., Chau, J. L., Weber, T., & Latteck, R. (2018). Enhancing the spatio-temporal features of polar mesosphere summer echoes using coherent MIMO and radar imaging at MAARSY. *Atmospheric Measurement Techniques Discussions*, *2018*, 1–23. https://doi.org/10.5194/amt-2018-258

Vadas, S. L., & Becker, E. (2018). Numerical modeling of the excitation, propagation, and dissipation of primary and secondary gravity waves during wintertime at McMurdo station in the Antarctic. *Journal of Geophysical Research: Atmospheres*, *123*, 9326–9369. https://doi.org/10.1029/2017JD027974

Vadas, S. L., Zhao, J., Chu, X., & Becker, E. (2018). The excitation of secondary gravity waves from local body forces: Theory and observation. *Journal of Geophysical Research: Atmospheres*, *123*, 9296–9325. https://doi.org/10.1029/2017JD027970

Vierinen, J. (2019). Kühlungsborn multi-static meteor radar campaign data, November2018, DataverseNO. https://doi.org/10.18710/PBYWJ0

Vierinen, J., Chau, J. L., Pfeffer, N., Clahsen, M., & Stober, G. (2016). Coded continuous wave meteor radar. *Atmospheric Measurement Techniques*, *9*(2), 829–839.

Vincent, R. A., & Reid, I. M. (1983). HF Doppler measurements of mesospheric gravity wave momentum fluxes. *Journal of the Atmospheric Sciences*, *40*(5), 1321–1333.

Vogelzang, Jur, King, GregoryP., & Stoffelen, A. (2015). Spatial variances of wind fields and their relation to second-order structure functions and spectra. *Journal of Geophysical Research: Oceans*, *120*, 1048–1064. https://doi.org/10.1002/2014JC010239

Yaglom, A. M. (1952). Introduction to the theory of stationary random functions. *Uspekhi Matematicheskikh Nauk*, *7*(5), 3–168.

Younger, P. T., Astin, I., Sandford, D. J., & Mitchell, N. J. (2009). The sporadic radiant and distribution of meteors in the atmosphere as observed by VHF radar at Arctic, Antarctic and equatorial latitudes. *Annales de Geophysique*, *27*, 2831–2841.

Erratum

In the originally published version of this article, Figure 1 was incorrect. Figure 1 has since been corrected, and this version may be considered the authoritative version of record.